

The Solar and Geomagnetic Storms in May 2024: A Flash Data Report

Hisashi Hayakawa (1 – 4)*, Yusuke Ebihara (5 – 6), Alexander Mishev (7 – 8), Sergey Koldobskiy (7 – 8), Kanya Kusano (1), Sabrina Bechet (9), Seiji Yashiro (10 – 11), Kazumasa Iwai (1), Atsuki Shinbori (1), Kalevi Mursula (8), Fusa Miyake (1), Daikou Shiota (1, 13), Marcos V. D. Silveira (14), Robert Stuart (15), Denny M. Oliveira (11 – 12), Sachiko Akiyama (10 – 11), Kouji Ohnishi (16), Yoshizumi Miyoshi (1)

- (1) Institute for Space-Earth Environmental Research, Nagoya University, Nagoya, Japan
- (2) Institute for Advanced Research, Nagoya University, Nagoya, Japan
- (3) Space Physics and Operations Division, RAL Space, Science and Technology Facilities Council, Rutherford Appleton Laboratory, Harwell Oxford, Didcot, UK
- (4) Astro-Glaciology Laboratory, Riken Nishina Centre, Wako, Japan
- (5) Research Institute for Sustainable Humanosphere, Kyoto University, Uji, Japan
- (6) Unit of Synergetic Studies for Space, Kyoto University, Kyoto, Japan
- (7) Sodankylä Geophysical Observatory, University of Oulu, Oulu, Finland
- (8) Space Physics and Astronomy Research Unit, University of Oulu, Oulu, Finland
- (9) Royal Observatory of Belgium, Brussels, Belgium
- (10) The Catholic University of America, Washington, DC, USA
- (11) NASA Goddard Space Flight Center, Greenbelt, MD, USA
- (12) Goddard Planetary Heliophysics Institute, University of Maryland, Baltimore County, Baltimore, MD, USA
- (13) National Institute of Information and Communications Technology, Japan
- (14) University of São Paulo, Lorena School of Engineering, Lorena, Brazil
- (15) Newtown Astronomical Society, Rhayader, UK
- (16) Center for Liberal Art, Department of Engineering, National Institute of Technology, 716 Tokuma, Nagano, 3818550, Japan

* hisashi@nagoya-u.jp

Abstract

In May 2024, the scientific community observed intense solar eruptions that resulted in an extreme geomagnetic storm and auroral extension, highlighting the need to document and quantify these events. This study mainly focuses on their quantification. The source active region (AR 13664) evolved from 113 to 2761 millionths of the solar hemisphere between 4 May and 14 May 2024. AR 13664's magnetic free energy surpassed 10^{33} erg on 7 May 2024, triggering 12 X-class flares. Multiple interplanetary coronal mass ejections (ICMEs) came out from this AR, accelerating solar energetic particles toward Earth. At least four ICMEs seemingly piled up to disturb the interplanetary space, according to the satellite data and interplanetary scintillation data. The shock arrival at 17:05 UT on 10 May 2024 significantly compressed the magnetosphere down to $\approx 5.04 R_E$, and triggered a deep Forbush decrease. GOES satellite data and ground-based neutron monitors confirmed a ground-level enhancement from 2 UT to 10 UT on 11 May 2024. The ICMEs induced extreme geomagnetic storms, peaking at a Dst index of -412 nT at 2 UT on 11 May 2024, marking the sixth-largest storm since 1957. The AE and AL indices showed extreme auroral extensions that located the AE/AL stations into the polar cap. We gathered auroral records at that time and reconstructed the equatorward boundary of the visual auroral oval to 29.8° invariant latitude. We compared naked-eye and camera auroral visibility, providing critical caveats on their difference. We also confirmed global enhancements of storm-enhanced density of the ionosphere.

1. Introduction

Sunspot active regions occasionally direct interplanetary coronal mass ejections (ICMEs) to the Earth, disrupting near-Earth space environments, altering cosmic-ray radiation levels, perturbing terrestrial magnetic fields, and extending the auroral oval equatorward (Pulkkinen, 2007; Temmer, 2021; Cliver *et al.*, 2022; Kusano, 2023; Usoskin, 2023). Empirical evidence suggests that such solar eruptions occur more often in larger solar cycles, especially from their maximum to the declining phase, whereas their maximum magnitudes are not necessarily dependent on the size of their host solar cycle (Kilpua *et al.*, 2015; Lefèvre *et al.*, 2016; Chapman *et al.*, 2020; Owens *et al.*, 2022; Chapman and Dudok de Wit, 2024). Extending analyses to the extremity of solar eruptions and their terrestrial consequences is essential to bridge modern scientific data with past supersized events, compare solar data with stellar data, and understand impacts on terrestrial infrastructure (Daglis, 2001; Baker *et al.*, 2008; Beggan *et al.*, 2013; Riley *et al.*, 2018; Miyake *et al.*, 2019; Hapgood *et al.*, 2021; Kusano, 2023; Usoskin *et al.*, 2023).

In this context, the last solar cycle, Solar Cycle 24 (SC24: from December 2008 to December 2019), was notably quiet in terms of disturbances in the solar-terrestrial environments (Watari, 2017; Manu *et al.*, 2022). This solar cycle (SC) marked the quietest sunspot number in the last century since Solar Cycle 14 in January 1902 – July 1913 (Clette *et al.*, 2023). Moreover, SC24 only witnessed up to X14.8 in September 2017 in the revised scale (Hudson *et al.*, 2024), geomagnetic storms reached a minimum Dst = -234 nT in March 2015 (Gopalswamy *et al.*, 2015, 2024; Liu *et al.*, 2015; Piersanti *et al.*, 2017; Webb and Nitta, 2017; WDC for Geomagnetism at Kyoto *et al.*, 2015), and hosted only two ground level enhancements (GLE) in May 2012 and September 2017 (Mishev *et al.*, 2014, 2018; Usoskin *et al.*, 2020).

The current solar cycle, Solar Cycle 25 (SC25), commenced in December 2019. Predictions suggest that this cycle may be either as quiet as or slightly more active than SC24 (Pesnell and Schatten, 2018; McIntosh *et al.*, 2020; Mursula, 2023; Upton and Hathaway, 2023; Clette *et al.*, 2024), whereas lessons from the previous cycle caution us to closely monitor how these forecasts align with the actual temporal evolution of the sunspot number (Pesnell, 2016, 2020). Despite these predictions, SC25 has shown increased activity compared to SC24 in terms of disturbances in terrestrial environments. Even prior to reaching its maximum, SC25 has already witnessed one severe geomagnetic storm (with a minimum Dst below -200 nT according to the classic classification of Loewe and Prölss (1997)) in April 2023, reaching a minimum Dst of -213 nT (Li and Jin, 2024), and one Ground Level Enhancement (GLE) event in October 2021 (Mishev *et al.*, 2022; Papaioannou *et al.*, 2022; Klein *et al.*, 2022).

In May 2024, SC25 witnessed the emergence of a significant sunspot active region, triggering multiple solar eruptions and leading to a Ground Level Enhancement (GLE) and a substantial geomagnetic storm. Notably, this geomagnetic disturbance ranked as the sixth greatest since 1957 according to the Dst index and the ninth greatest according to the Dxt index since 1932 according to the Dxt index (WDC for Geomagnetism at Kyoto *et al.*, 2015; Karinen and Mursula, 2005; Mursula *et al.*, 2023). This geomagnetic storm extended auroral displays to lower magnetic latitudes (*e.g.*, Ghosh, 2024; Greshko, 2024). This solar-terrestrial storm serves as a valuable reference point for connecting modern scientific data with past extreme events, particularly regarding geomagnetic impacts. Here, we quantify observational datasets from this solar-terrestrial storm to facilitate further analysis and discussions regarding this exceptional event and to contextualise it with historical extreme events.

2. The Source Solar Eruptions

This event occurred in an ascending phase – or near the maximum – of SC25. The daily sunspot number (Clette *et al.*, 2023) significantly increased on 2 May, reaching 187 on 6 May and 186 on 12 May. At the time of writing, some predictions place the expected maximum from late 2024 to early

2025 (McIntosh *et al.*, 2021; Upton *et al.*, 2023; Clette *et al.*, 2024), whereas we must follow up how these predictions satisfy the actual temporal evolution of the sunspot number, according to lessons from the previous SC (Pesnell, 2016, 2020).

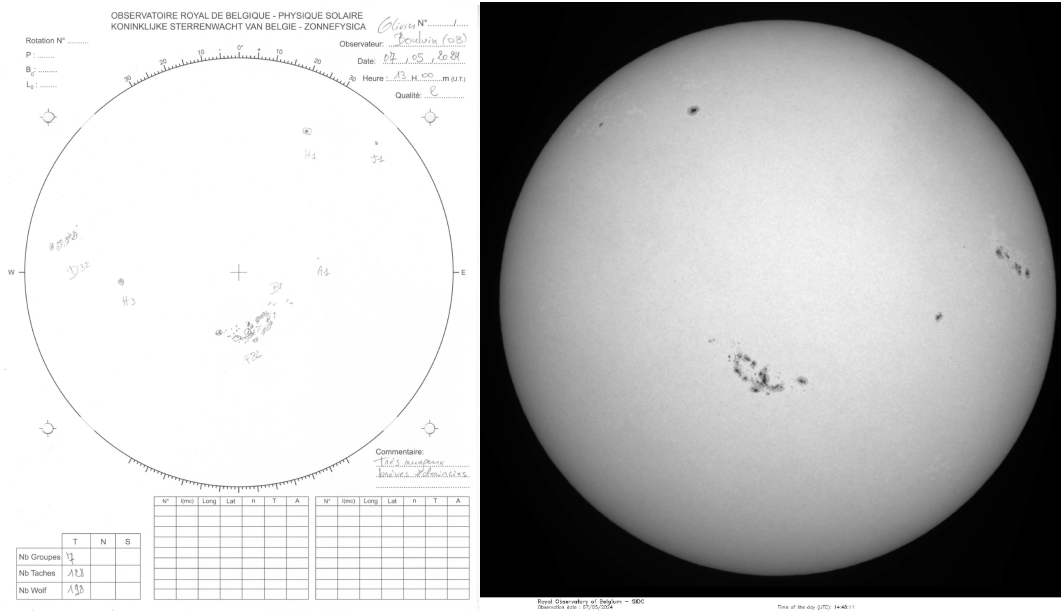


Figure 1: Sunspot drawing and white-light image on 07 May 2024, as recorded with Uccle Solar Equatorial Table telescopes in the Royal Observatory of Belgium. NOAA 13664 is located close to the central meridian.

A new active region (AR), known as AR 13664 according to the NOAA/SWPC region number, came into the south-eastern limb of the visible side of the solar disk on 1 May. Its temporal and spatial evolutions were documented in sunspot drawings and images in several observatories such as the Royal Observatory of Belgium using the Uccle Solar Equatorial Table (USET) telescopes (Bechet and Clette, 2022). This sunspot group started as a bipolar group, with two penumbrae and some intermediate sunspots in between. This active region developed rapidly from 3 May–7 May. It crossed the central meridian on 7 May. The area measured from the USET sunspot drawing was 1312 millionths of the visible solar hemisphere (hereafter MSH), based on the measurements with the Digi Sun software (*e.g.*, Clette, 2011; Hayakawa *et al.*, 2023c). This group was still growing and developed into a Fkc McIntosh type, consisting of several moderately sized penumbral sunspots. This group continued to grow until 9 May up to an area of 2761 MSH, consisting of a compact penumbra containing most of the spots, as shown in the sunspot drawing and white-light image (Figure 1). The area remained relatively stable for a period before rotating over the limb on 14 May. The evolution of the group area, as measured from sunspot drawings, is illustrated in Figure 2, showing a rapid increase until 10 May.

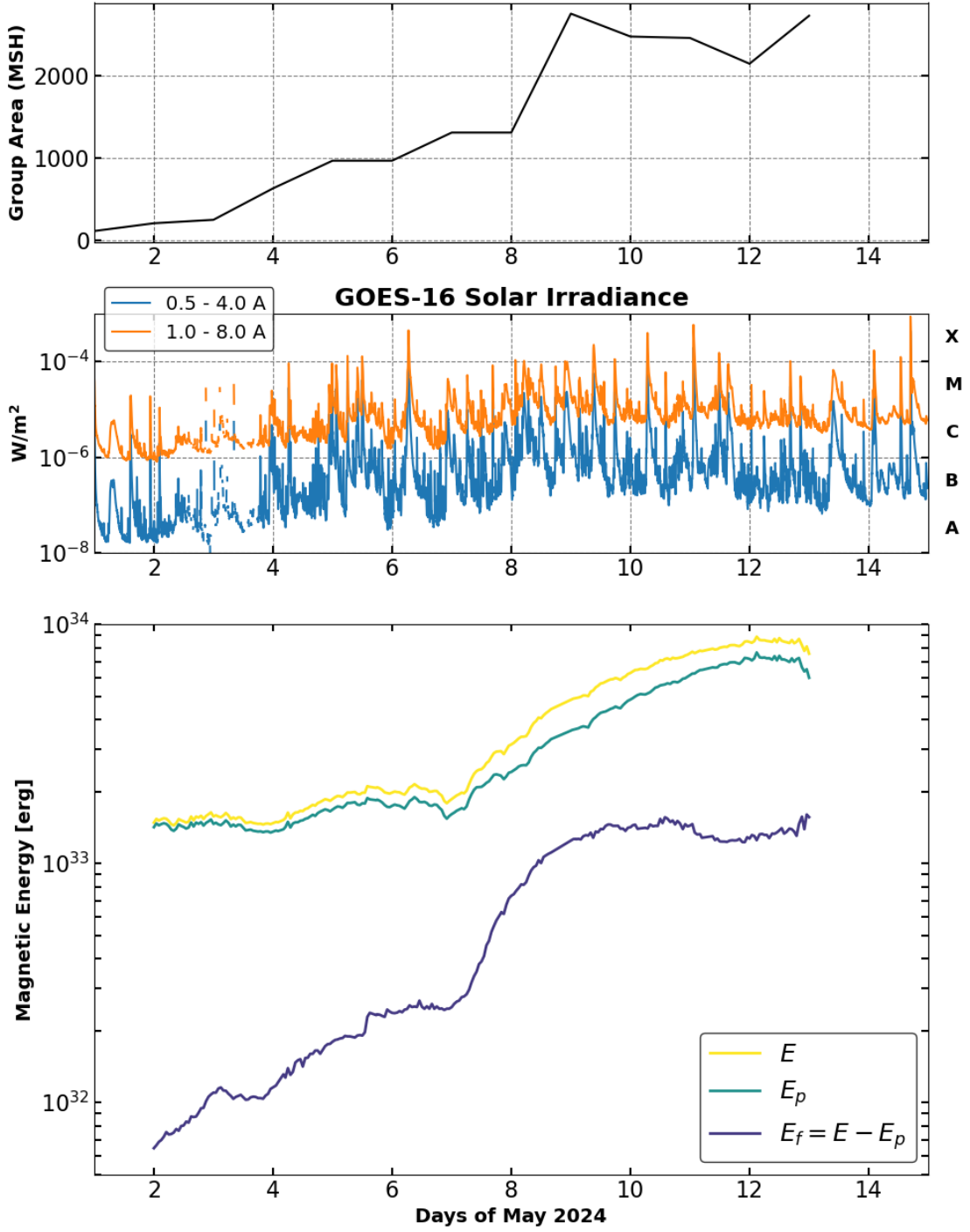


Figure 2: Temporal evolutions of the AR 13664 in millionths of the visible solar hemisphere (MSH) based on the USET measurements, GOES-16 X-ray fluence in 0.5–4.0 Å and 1.0–8.0 Å, as derived from the NOAA web portal, and the magnetic energy of the active region NOAA 13664 as a function of the day of May 2024. E , E_p , and E_{free} are the total energy of the nonlinear force-free field, the potential magnetic field, and the free magnetic energy ($E - E_p$).

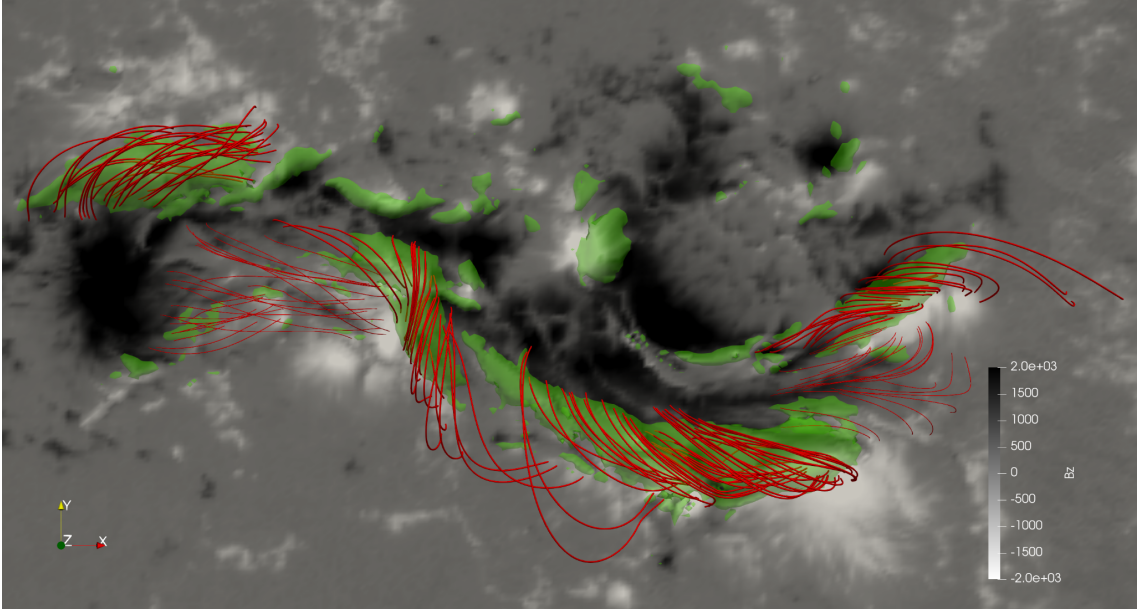


Figure 3: The distribution of the magnetic field of AR 13664 at 06:00 UT on 10 May 2024, just before the X3.9 flare. The grayscale background indicates the radial magnetic field (B_z [G]), and the green surface is the contour of 10^3 G for the nonpotential field intensity, corresponding to HiFERS. Red lines show selected magnetic field lines of the nonlinear force-free field.

The unsigned magnetic flux constantly increased from 7 May to 1.9×10^{23} Mx before it reached the west limb. We extrapolated the nonlinear force-free field (NLFFF) (Inoue *et al.*, 2014) of this AR using near-real-time data of the photospheric vector magnetic field from the Spaceweather HMI Active Region Patch (SHARP) near-real-time (NRT) dataset (Bobra *et al.*, 2014). Figure 2 shows the magnetic free energy, which is defined as the difference between the volume-integrated magnetic energy of the NLFFF and the potential magnetic field. We can see that the magnetic free energy increased before the M-class flares on 2 May and quickly grew on 7 May to $\approx 10^{33}$ erg before the consecutive X-class flares (Figure 2 and Table 1). The maximum values of the unsigned magnetic flux and magnetic free energy are as large as those of AR NOAA 12192, which provides the largest sunspot area, unsigned flux, and magnetic free energy in SC 24 (Karimov *et al.*, 2024).

Figure 3 shows the distribution of the radial magnetic field and the contours of nonpotential magnetic field intensity $|\mathbf{B} - \mathbf{B}_p| = 1000$ G (green surfaces), where \mathbf{B} and \mathbf{B}_p are the magnetic fields from the SHARP-NRT data and the potential magnetic field. Red lines are the magnetic field lines of force for the nonlinear force-free field extrapolated by the magnetohydrodynamic (MHD) relaxation method (Inoue *et al.*, 2014). The notable feature of this region is the presence of several high free energy regions (HiFERS) where the nonpotential field intensity exceeds 1000 G. Likely, the large free energy and the complex structure of the HiFERS distribution may cause consecutive large flares (Kusano *et al.*, 2020).

Eventually, this active region hosted 12 X-flares from 1 May to 15 May (Table 1 and Figure 2). Most of these are produced during transit over the visible solar hemisphere, while four were produced after the AR went over the western limb and came into the far side. This AR produced a flare as great as X8.7. Even though the flare partially occurred on the western limb, this was the largest solar flare in the current solar cycle (SC25) at the time of writing. Figure 2 shows the soft X-ray flux continuously above the M1 level from 8 to 12 May.

Table 1: Summary of the X-class flare produced by the AR 13664, with their peak time, GOES class, source location and associated CME (if any). The flare magnitudes and source locations are derived from the Event Archives of Solar Software of the Lockheed Martin Solar & Astrophysics Laboratory

with a minor modification for location of the limb eruptions. We have annotated the longitude of the limb flares on the western limb as WL, in contrast with the Event Archives of Solar Software. The CME (coronal mass ejection) speeds in km/s are derived from the SOHO/LASCO data based on Gopalswamy *et al.* (2024, in preparation). Their travel time (in hh:mm) and arrival time are estimated under assumption of no deceleration of the CME speed in the fifth column as measured in the SOHO/LASCO data. We have estimated their travel time and arrival time for the CMEs originated from the central meridian ($< |45|^\circ$ in from the central meridian).

ID	GOES peak time	GOES class	Location	CME speed	Travel time*	Arrival time*
1	2024-05-08 05:09	X1.0	S22 W11	511	82:08	05-11 15:17
2	2024-05-08 21:40	X1.0	S20W17	947	44:19	05-10 17:00
3	2024-05-09 09:13	X2.2	S20 W24	1226	34:14	05-10 19:27
4	2024-05-09 17:44	X1.1	S17 W28	1019	41:11	05-11 10:53
5	2024-05-10 06:54	X3.9	S17 W34	1006	41:43	05-12 00:37
6	2024-05-11 01:23	X5.8	S17 W44	1512	27:45	05-12 05:08
7	2024-05-11 11:44	X1.5	S19 W60	No CME	--	--
8	2024-05-12 16:26	X1.0	S20 W75	No CME	--	--
9	2024-05-14 02:09	X1.7	S17 WL	929	--	--
10	2024-05-14 12:55	X1.2	S17 WL	792	--	--
11	2024-05-14 16:51	X8.7	S18 WL	1988	--	--
12	2024-05-15 08:37	X3.4	S18 WL	1724	--	--

3. Coronal Mass Ejections

These solar eruptions released considerable coronal mass ejections (CMEs). During 5 – 15 May 2024, the Large Angle Spectroscopic Coronagraph (LASCO) observed at least 19 major CMEs (width $\geq 60^\circ$) including 10 halo CMEs, which were produced by AR 13664 (Gopalswamy *et al.* 2024, in preparation). Although the calibrated LASCO data are not available at the time of writing, the CME properties were measured using level zero quick-look data by the same procedure of the CDAW (Coordinated Data Analysis Workshops) CME Catalog (Yashiro *et al.*, 2004; Gopalswamy, 2009).

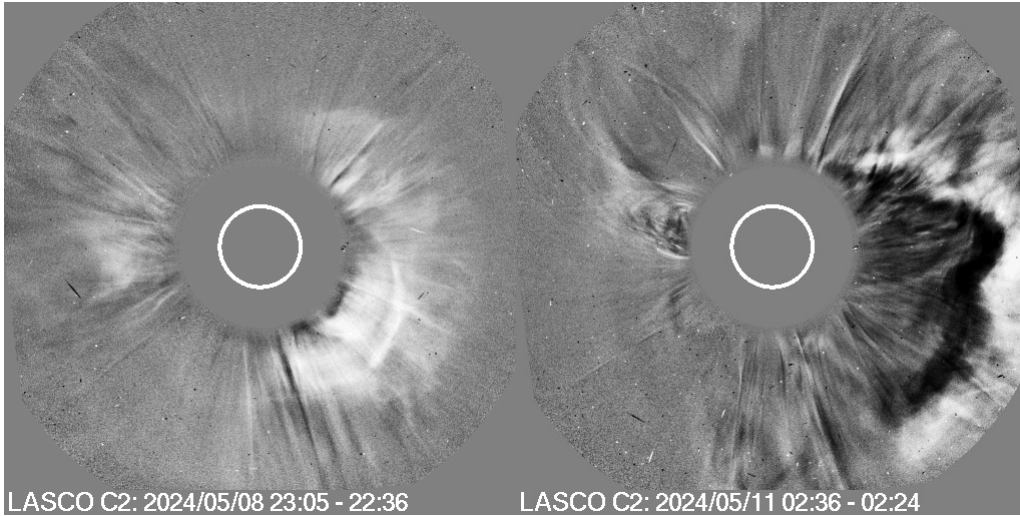


Figure 4: Examples of halo CMEs from AR 13664, as observed by LASCO C2 (Brueckner *et al.*, 1995) at 22:36 – 23:05 on 8 May 2024 (left) and 02:24 – 02:36 on 11 May 2024 (right), with image courtesy of the CDAW of the NASA.

We attempted to identify the CME most probably responsible for the start of observed space environment disturbances near Earth. At the end of 8 May, two flares (X1.0 at 21:40 UT and M9.8 at 22:27 UT) occurred in quick succession. Their erupting features were observed by SDO/AIA (Solar Dynamics Observatory/Atmospheric Imaging Assembly (Lemen *et al.*, 2012)). However, only a single halo CME was observed at 22:24 UT (#2 in Table 1; hereafter CME2), as shown in Figure 4. Likely, the two eruptions seen in AIA were merged before reaching the LASCO C2 field of view. The projected speed of this halo CME was 947 km/s. If CME2 travels with the projected speed without any deceleration, it is estimated to arrive at the Earth around $\approx 17:00$ UT on 10 May (shown in Table 1). On their basis, the CME2 is probably associated with the Storm Sudden Commencement (SSC) at 17:05 on 10 May. The estimated arrival times indicate that CME2 probably piled up on CME1. Other than CME1, two more halo CMEs were observed. They are associated with M-class flares (Table 2) in AR 13664. CME2 probably collided and piled up with three preceding CMEs originated from the same AR (AR 13664), resulting in the complex ICME structure (described in later). On their basis, the extreme geomagnetic storm on 10/11 May 2024 is not associated with a single fast ICME but with a complex pileups of multiple ICMEs and southward interplanetary magnetic field (IMF).

Table 2: Major CMEs observed in the Large Angle Spectroscopic Coronagraph (LASCO) from the AR 13664 (Gopalswamy *et al.* 2024, in preparation). This table shows date, starting time, speed, and angular width (WD) for the CMEs, flare starting time and GOES X-ray class, location, and NOAA AR number for the solar sources. We have annotated the limb eruption as WL for their source location.

Date	CME time	CME speed	CME WD	Flare time	Flare class	Location	NOAA
2024-05-05	15:36	549	121	14:12	C7.5	S20E19	13664
2024-05-07	04:48	389	78	02:59	C9.5	S21E05	13664
2024-05-08	02:24	360	142	02:16	M3.4	S17W04	13664

2024-05-08	05:36	511	360	04:37	X1.0	S22W11	13664
2024-05-08	12:24	798	360	11:26	M8.7	S20W17	13664
2024-05-08	22:36	947	360	21:08	X1.0	S20W17	13664
2024-05-09	09:24	1226	360	08:45	X2.2	S20W26	13664
2024-05-09	12:24	833	123	11:52	M3.1	S16W40	13664
2024-05-09	19:18	1019	360	17:23	X1.1	S14W28	13664
2024-05-10	07:12	1006	360	06:27	X3.9	S17W34	13664
2024-05-11	01:36	1512	360	01:10	X5.8	S15W45	13664
2024-05-11	16:12	970	87	14:46	M8.8	S15W49	13664
2024-05-13	09:12	1812	360	08:48	M6.6	S20W81	13664
2024-05-14	01:48	341	68	01:23	M2.6	S17W88	13664
2024-05-14	02:24	929	87	02:03	X1.7	S19W88	13664
2024-05-14	13:00	792	55	12:40	X1.2	S17W92	13664
2024-05-14	17:00	1988	196	16:46	X8.7	S18W96	13664
2024-05-15	08:36	1724	360	08:13	X3.5	S18W98	13664
2024-05-15	10:48	1045	69	09:47	M3.6	WL	13664
2024-05-15	21:18	1359	360	20:30	C5.2	WL	13664

Subsequently, this AR launched additional halo CMEs. Two major flares (X1.1 at 09:24 on 9 May and X3.8 at 07:12 on 10 May) launched ICMEs with a similar speed (1226 km/s and 1006 km/s). One more major flare (X5.8 on 01:36 on 11 May) launched a faster ICME (1512 km/s), as shown in Figure 4. These ICMEs probably arrived at the Earth around 9 UT on 12 May. This short difference between the observed arrival times and the estimated arrival times shown in Table 1 may imply that this preceding sequence of ICMEs cleaned up the interplanetary space and allowed subsequent ICMEs to propagate the interplanetary space without much deceleration (*e.g.*, Shiota and Kataoka, 2016). These ICMEs kept the solar wind compressed and the resultant geomagnetic storm lived longer.

In general, CME speeds can be higher than projected ones or lower owing to the deceleration during

propagation. Therefore, the actual arrival time most probably has a variation from the estimated arrival time in our Table 1. Furthermore, the AR 13664 caused multiple CMEs with much different speeds within a few days. Therefore the correspondence relationship between CMEs observed in coronagraphs and ICME structures observed in situ can be much more complex. In order to interpret their relationship, further analyses are prepared for the MHD simulation of multiple CME propagations. Owing to their complexity, further in-depth analyses are currently under preparation for interplays of these ICMEs (*e.g.*, Shiota *et al.*, 2024 in prep).

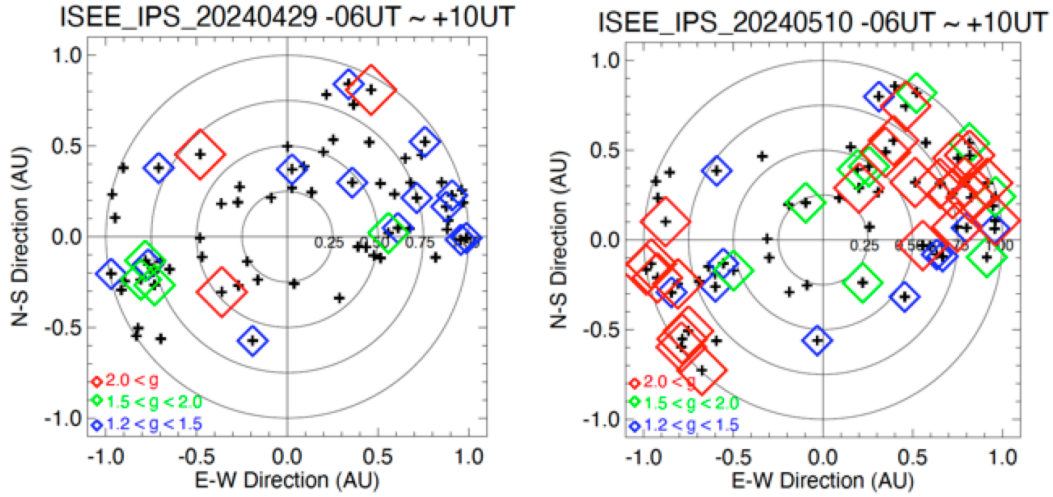


Figure 5: All-sky map of the IPS amplitude (g value) observed by ISEE, Nagoya University on (a) April 29 when the AR 13663 was not on the disk and (b) May 10, 2024. The symbols indicate +: all observed radio sources, diamonds: radio sources with g values as follows: $2.0 < g$ (red), $1.5 < g < 2.0$ (green) and $1.2 < g < 1.5$ (blue).

When ICMEs cross the line of sight upon observation of radio sources out of the solar system, their crossing scatters radio emissions from the radio source and is observed as an interplanetary scintillation (IPS). IPS observations have been used to study ICMEs in the interplanetary space between the coverages of the SOHO view and geospace space satellites located around L1. Here, we have analysed IPS observational data in early May according to the measurements of the ISEE, Nagoya University at 327 MHz (Tokumaru *et al.*, 2011). The IPS observations in early May have allowed us to detect an increasing number of large-amplitude IPS responses on 8–10 May, just before the shock arrival at the Earth (Figure 5). Figure 5 shows detections of large-amplitude IPS responses in numerous radio sources, especially in the line of sight in the direction of large solar separation angles, where the ICMEs in question were supposed to be located. Enhancements on IPS responses can be associated with the high-density region where the fast-propagating ICMEs pile up the background solar wind (Iwai *et al.*, 2019, 2021). Multiple ICME merging can enhance compression of the solar wind plasma (Scolini *et al.*, 2020). ICME compressions can produce intense radio scattering if a region of concentrated density disturbances is created (Equation 1 of Iwai *et al.* (2019); see also Young (1971)). This may support our discussions on the ICME-ICME interaction shown above. Further in-depth analyses are needed and hence going on under Iwai *et al.* (2024, in prep).

4. Cosmic Ray Variations in Near-Earth Space and on the Ground

To monitor the cosmic ray intensity around this solar-terrestrial storm, we gathered solar proton flux data from the eastern and western monitors of the Solar and Galactic Proton SGPS onboard the GOES-16 satellite (Kress *et al.*, 2021) downloaded from the NOAA data portal. We also acquired ground-based NM records from high-latitude regions, namely those of Oulu (Oulu in Finland),

THUL (Thule in Greenland), SOPO (South Pole in Antarctica), and MWSN (Mawson in Antarctica), from the Oulu NM website and the Neutron Monitor Database, as summarised in the IGLED (Usoskin, 2020). These data are summarised in Figure 6 with their source URLs.

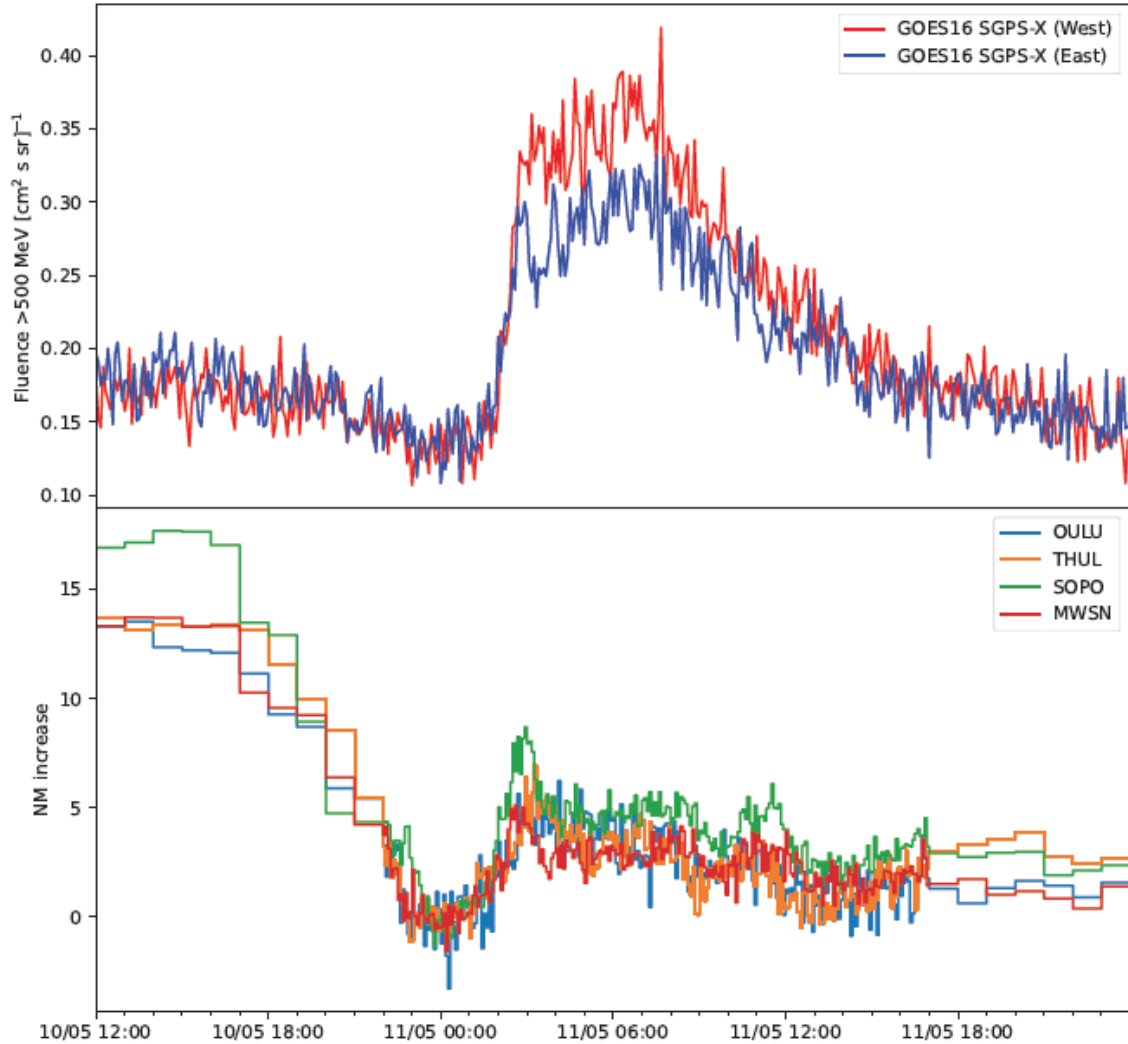


Figure 6: Cosmic Ray Flux >500 MeV observed by eastern- and western-facing monitors of the SGPS detector onboard the GOES-16 satellite, based on NOAA data portal¹, alongside the increase in ground-based neutron monitor count rates from high-latitude regions. The neutron monitor sites include Oulu (located in Finland at N65°03', E025°28', 15 m above sea level), THUL (located in Thule, Greenland, at N76°30', W068°42', 26 m above sea level), SOPO (located at the South Pole in Antarctica, at S90°00', N/A, 2820 m above sea level), and MWSN (located at Mawson in Antarctica, at S67°36', E062°53', 30 m above sea level), as sourced from the Oulu Neutron Monitor² and Neutron Monitor Database³, and summarised in the International Ground Level Enhancement Database⁴ (IGLED). All data are corrected for barometric pressures without a detrending procedure. For neutron monitor increase calculations, the baseline was selected from 23:00 on 10 May to 01:00 on 11 May for MWSN, SOPO, and THUL, and from 23:30 on 10 May to 01:30 on 11 May for Oulu.

¹ <https://data.ngdc.noaa.gov/platforms/solar-space-observing-satellites/goes/goes16/12/data/sgps-12-avg5m>

² <https://cosmicrays oulu.fi/>

³ <https://www.nmdb.eu/nest/>

⁴ <https://gle oulu.fi/#/>

During the period under investigation in this study, specifically on 10 – 11 May 2024, we observed a significant variation in CR activity. Corresponding to the arrival of CMEs at 17:05 UT, as shown by the sudden storm commencements (SSC) in the Kakioka Observatory (Kakioka Magnetic Observatory, 2013, see details in Section 6), a significant Forbush decrease (FD) (Forbush, 1937) in CR intensities was observed in all available datasets with different cutoff rigidities. The maximum decrease in the NM count rate of magnitude $\geq 15\%$ or more was reached around midnight, after which the recovery phase began.

Around 2 UT on 11 May flux of high-energy (>500 MeV) protons started to increase as registered by the GOES-16 satellite (Figure 6). Accordingly, the significant changes in the solar proton flux triggered several alerts by the Bartol group, as well as by GLE alert++ by the Athens CR group, and also by the Kazakhstan CR group, issuing an alert signal at 01:55 UT (private communication with O. Kraykunova). However, the two latter alerts were produced using several mid-latitude stations and are likely due to a reduction in the cutoff rigidity resulting from strong magnetospheric storms (Kudela *et al.*, 2008). Detailed NM records are provided in the Neutron Monitor Database (Mavromichalaki *et al.*, 2011) and International GLE database (Usoskin, 2020). According to a careful inspection of the records, polar NMs, such as the South Pole, Thule, Oulu, and Mawson (Figure 6), exhibit a small increase from ≈ 2 UT to 10 UT during the recovery of the deep FD, whose profile corresponds to the SEP profile registered by the SGPS onboard the GOES-16 satellite. Since the cutoff rigidity of these NM stations is nearly zero, the magnetospheric effect, that is, the reduction of the cutoff rigidity, cannot be used to explain the count rate increase.

Therefore, according to the recently updated ground level enhancement (GLE) definition: “A GLE event is registered when there are near-time coincident and statistically significant enhancements of the count rates of at least two differently located high-elevation neutron monitors and a corresponding enhancement in the proton flux measured by a space-borne instrument(s)” (for details see Poluianov *et al.*, 2017, and the discussion therein), the global NM network observed a GLE. Therefore, this event was confirmed as GLE #74, the second of the current Solar Cycle 25, after GLE #73 on 28 October 2021 (Papaioannou *et al.*, 2022; Mishev *et al.*, 2022). and was included in the International GLE Database. As discussed above, the NM count rate increases during this event are a complicated interplay between the recovery of the FD, increased SEP flux, and geomagnetic storm impact; the former plays a role at polar stations and the latter at mid- and low-latitude stations. A detailed analysis of this complex event is desired and reserved for further dedicated studies.

5. Interplanetary Shock Arrivals and Magnetospheric Compressions

In this section, we used measurement datasets of THEMIS (Time History of Events and Macroscale Interactions during Substorms) spacecraft (Angelopoulos, 2008) to evaluate the magnetospheric compressions upon the shock arrival. We have derived the magnetic field measurements from the fluxgate magnetometers (FGM) (Auster *et al.*, 2008) and the ion moments from the electrostatic analyzer (ESA) (McFadden *et al.*, 2008). On 10 May 2024, upon the arrival of the interplanetary (IP) shock, all three THEMIS satellites were positioned in alignment within the post-noon sector of the dayside magnetosphere performing an inbound orbit.

Figure 7 shows THEMIS-E measurements for the magnetic field and plasma during the interval between 17:04 UT and 17:07 UT. From top to bottom, Figure 7 shows the magnetic field strength (B_{total}), the magnetic field components (B_x , B_y , B_z) in Geocentric Solar Ecliptic (GSE) coordinate system, ion energy flux spectrogram, bulk flow velocity (V_x , V_y , V_z) in GSE, and number density (N_i). The spacecraft position in GSE is annotated at the lower part of the plot. A vertical dashed line denotes the moment of magnetopause crossing (17:05 UT) at $[x, y, z]$ coordinate in Earth’s radii (R_E) of $[7.1, 3.2, -2.7]$ R_E . This indicates THEMIS-E’s crossing over the magnetopause as $\approx 8.24 R_E$. Figure 7 characterises the magnetopause with sudden offsets in all parameters in magnetic field and

plasma, particularly in the particle energy dispersion. Preceding the magnetopause, there is a period of stable magnetic field with positive B_z component, accompanied by low bulk flow velocity and a concentrated population of high-energy ions (> 1 keV), typical observations within Earth's magnetosphere. The region between the dashed and the solid lines corresponds to the magnetosheath, characterised by a decrease of the magnetic field, broader ion energy spectrum, and high values of the ion number density. Subsequent to the solid line, indicates the THEMIS-E transition into the solar wind, characterised by a high plasma flow velocity and a narrow ion energy spectrum around 1 keV.

Figure 8 shows THEMIS-A measurements for the magnetic field and plasma between 17:04 and 17:07 UT. This dataset independently confirms the said estimate. A vertical dashed line denotes the moment of magnetopause crossing (17:05 UT) at $[x, y, z]$ coordinate in Earth's radii (R_E) of $[7.7, 2.4, -2.7] R_E$. This indicates THEMIS-A's crossing over the magnetopause as $\approx 8.51 R_E$. This result is broadly consistent with THEMIS-E's crossing over the magnetopause as $\approx 8.24 R_E$.

Figure 9 shows THEMIS-E's measurements on magnetic field and plasma data in the same arrangements with Figure 7. In this case, the spacecraft is crossing from the magnetosheath to the magnetosphere, encountering the magnetopause of $[x, y, z]$ coordinate in R_E as $R_E = [3.4, 3.2, -1.9]$, denoted by the dashed line around 19:12 UT. This indicates THEMIS-E's crossing over the magnetopause as $\approx 5.04 R_E$. Initially, the magnetic field presents a very intense negative B_z component, subsequently undergoing a significant rotation in the B_z component while being still within the magnetosheath. The ion bulk flow velocity also experiments with high values and fluctuations in this region. Furthermore, a wider ion energy spectrum is also discernible. Upon entering the magnetospheric region, the magnetic field was still strong but devoid of high-frequency disturbances. The ion bulk velocity is much lower, as expected for magnetosphere plasma. Nevertheless, the number density persists at levels higher than the norm.

This compressed magnetopause value ($\approx 5.04 R_E$) is somewhat extreme, being smaller than the geosynchronous orbit ($6.6R_E$). However, THEMIS-A provides us with another independent credit to this estimate. Figure 10 shows THEMIS-A measurements for the magnetic field and plasma between 18:50 and 19:30 UT. A vertical dashed line denotes the moment of magnetopause crossing (19:19 UT) at $[x, y, z]$ coordinate in Earth's radii (R_E) of $[4.0, 2.9, -2.1] R_E$. This indicates THEMIS-A's crossing over the magnetopause as $\approx 5.37 R_E$. This result is broadly consistent with THEMIS-E's crossing over the magnetopause as $\approx 5.04 R_E$. Here, we have taken the entrance in the magnetosphere into account, when the energy of the main particle population is higher than 1 keV and there is an absence of particles from the magnetosheath, typical of the magnetosphere. The period preceding the dashed lines present particles spanning a wide range of energies, a mixture of magnetosphere and magnetosheath plasma. This region can be identified as a boundary layer characterised by open magnetic field lines. Overall, these measurements confirm considerable compressions of the magnetosphere immediately after the shock arrival at 17:05 UT. Further assessment is needed for this extreme case of the magnetospheric compression.

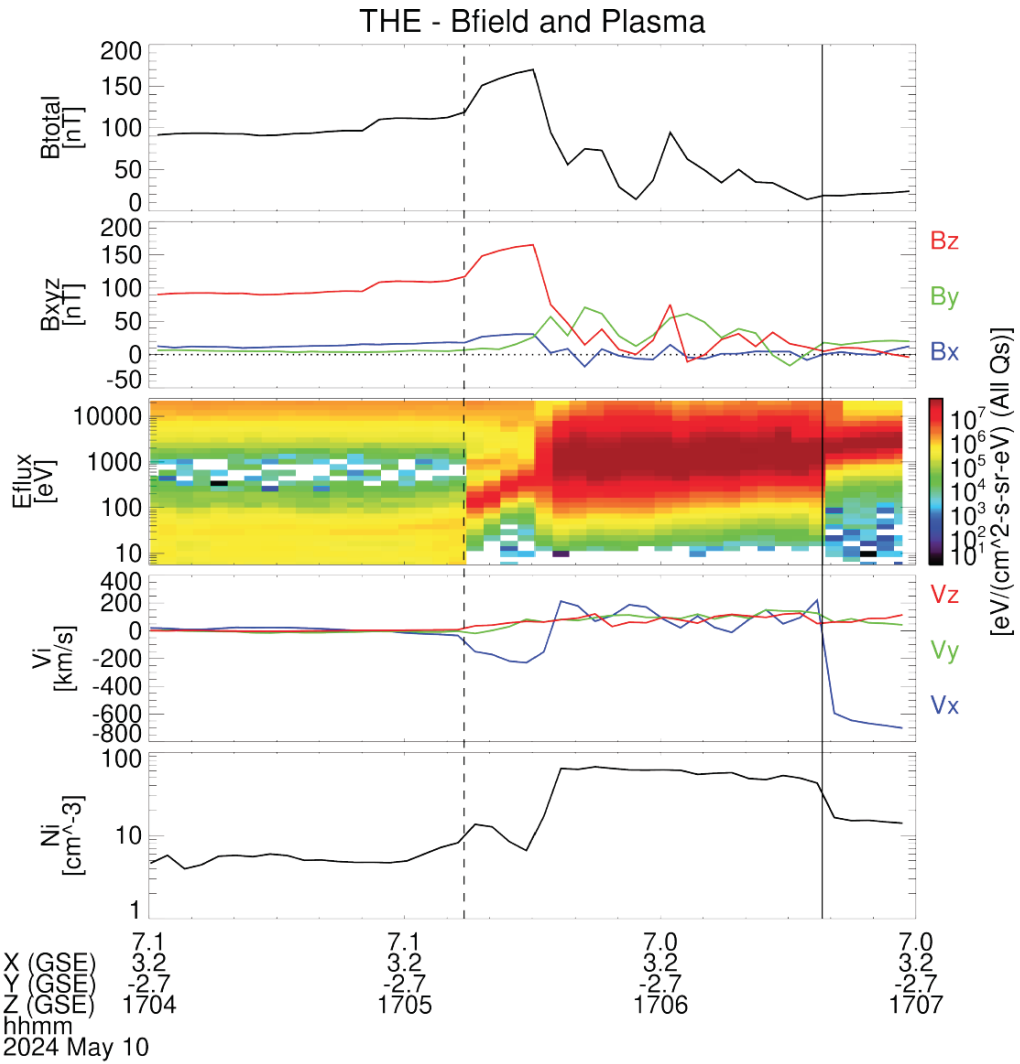


Figure 7: THEMIS-E's measurements between 17:04 and 17:07 UT for magnetic field strength (B_{total}), the magnetic field components (B_x , B_y , B_z) in Geocentric Solar Ecliptic (GSE) coordinate system, ion energy flux spectrogram, bulk flow velocity (V_x , V_y , V_z) in GSE, and number density (N_i). The magnetopause crossing is indicated with a vertical dashed line.

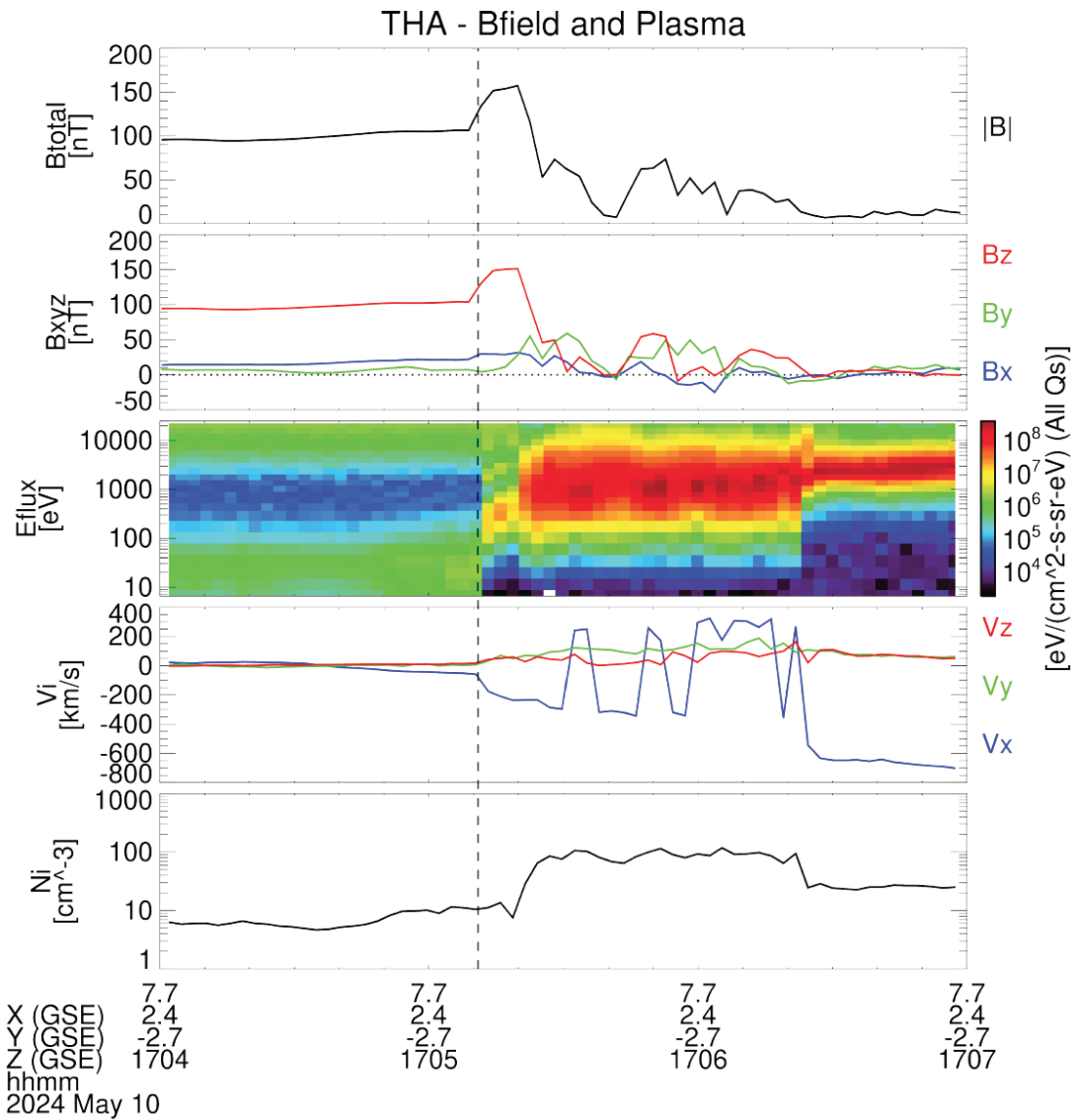


Figure 8: THEMIS-A's measurements between 17:04 and 17:07 UT for magnetic field strength (B_{total}), the magnetic field components (B_x , B_y , B_z) in Geocentric Solar Ecliptic (GSE) coordinate system, ion energy flux spectrogram, bulk flow velocity (V_x , V_y , V_z) in GSE, and number density (N_i). The magnetopause crossing is indicated with a vertical dashed line.

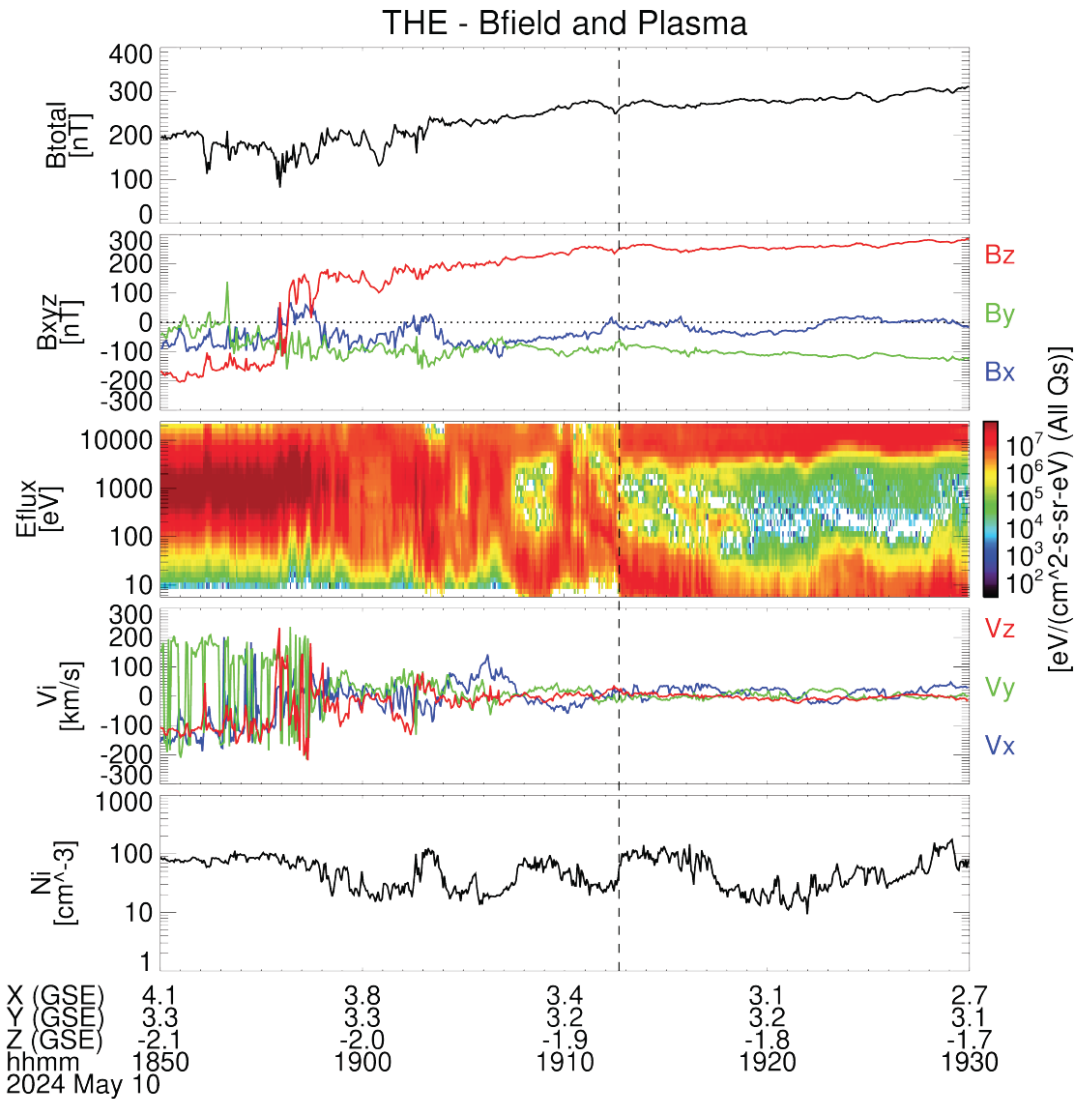


Figure 9: THEMIS-E's measurements between 18:50 and 19:30 UT for magnetic field strength (B_{total}), the magnetic field components (B_x , B_y , B_z) in Geocentric Solar Ecliptic (GSE) coordinate system, ion energy flux spectrogram, bulk flow velocity (V_x , V_y , V_z) in GSE, and number density (N_i). The magnetopause crossing is indicated with a vertical dashed line.

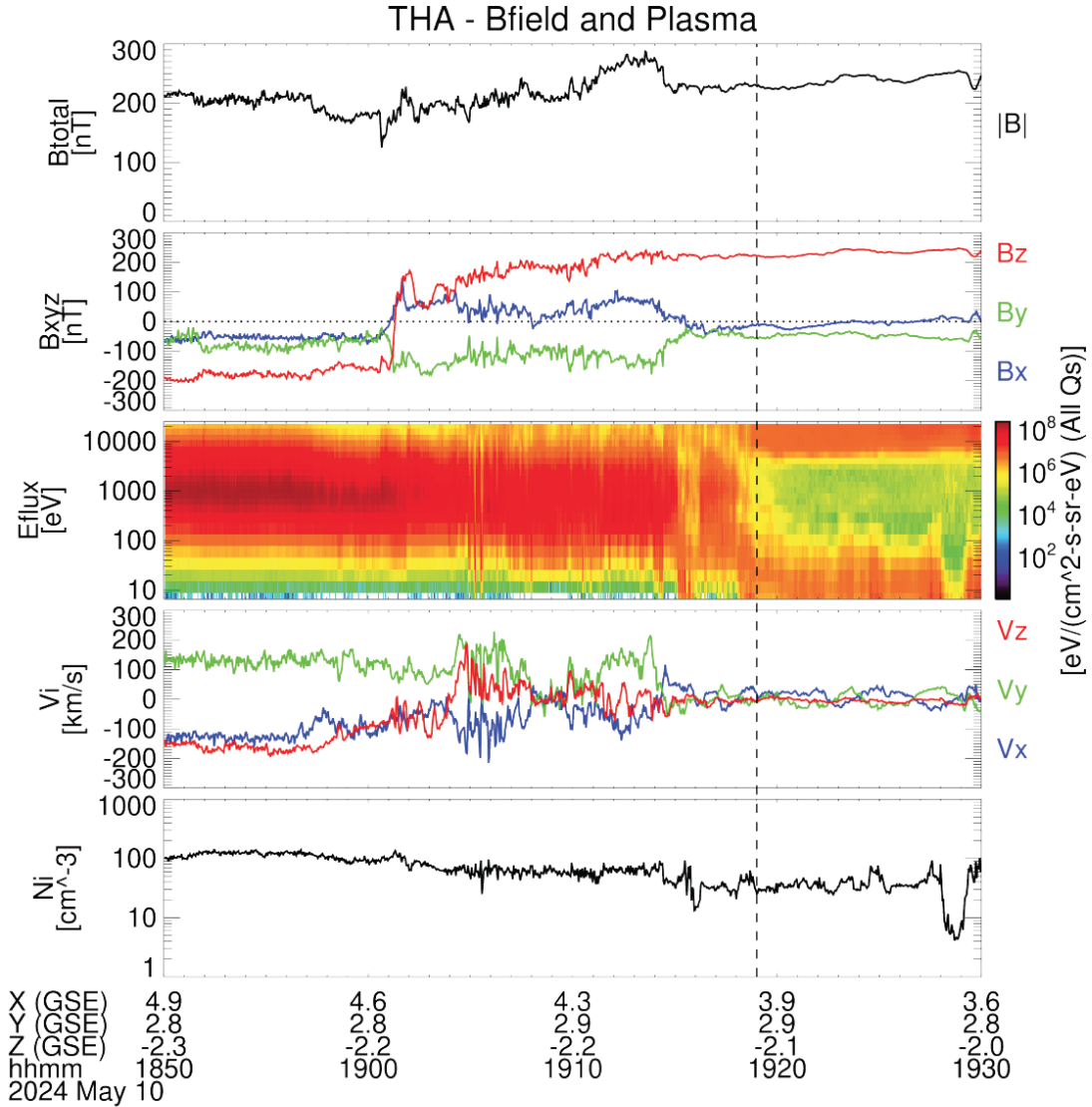


Figure 10: THEMIS-A's measurements between 18:50 and 19:30 UT for magnetic field strength (B_{total}), the magnetic field components (B_x , B_y , B_z) in Geocentric Solar Ecliptic (GSE) coordinate system, ion energy flux spectrogram, bulk flow velocity (V_x , V_y , V_z) in GSE, and number density (N_i). The magnetopause crossing is indicated with a vertical dashed line.

6. Geomagnetic Disturbances

The geomagnetic measurements captured at least four SSCs in May 2024. The Kakioka ΔH measurement recorded SSCs at $\approx 14:07$ UT on 2 May (26 nT), 17:05 UT on 10 May (78 nT), 05:51 UT on 16 May (10 nT), and 13:26 UT on 17 (18 nT), respectively (Kakioka Magnetic Observatory, 2015). Among them, it is the SSC at 17:05 UT on 10 May that triggered the extreme geomagnetic storm that we are discussing in our article. According to the real-time solar wind data acquired by ACE, a jump in solar wind speed and density arrived at the L1 Lagrange point at 16:36 UT on 10 May. In the vicinity of the jump, the speed increased from approximately 460 to 660 km/s, and the density increased from ≈ 10 to 27 cm^{-3} . This jump caused a substantial SSC from $\approx 17:05$ UT on 10 May up to ≈ 78 nT in the Kakioka ΔH measurement (Kakioka Magnetic Observatory, 2015). This implies that the travel time from the L1 point to Earth is 29 min at the SSC moment. This estimate includes the transition time from the magnetopause to the ground.

Figure 11 summarises ΔX observed at $20^\circ < \text{MLAT} < 30^\circ$ around the SSC. Again, ΔX at 17:04 UT on 10 May 2024 is set to be zero as a baseline. Abrupt increase in ΔX is evident at 17:05 – 17:06 UT. The SSC amplitude of the abrupt increase in ΔX is larger on the duskside than on the dawnside. This is consistent with the previous studies and attributed to the contribution from the magnetospheric current and the ionospheric current as well (*e.g.*, Araki *et al.*, 2006). The European sector witnessed a relatively large SSC amplitude, as it was located in the dusk side in the summer hemisphere upon the SSC. This favourable location probably enhanced ionospheric conductivity and the field-aligned current to increase the magnetic variations in the European sector (Shinbori *et al.*, 2009, 2012). The amplitude is ≈ 130 nT, which is large but not unique in comparison with the historical records of SSC (Araki, 2014; Hayakawa *et al.*, 2022).

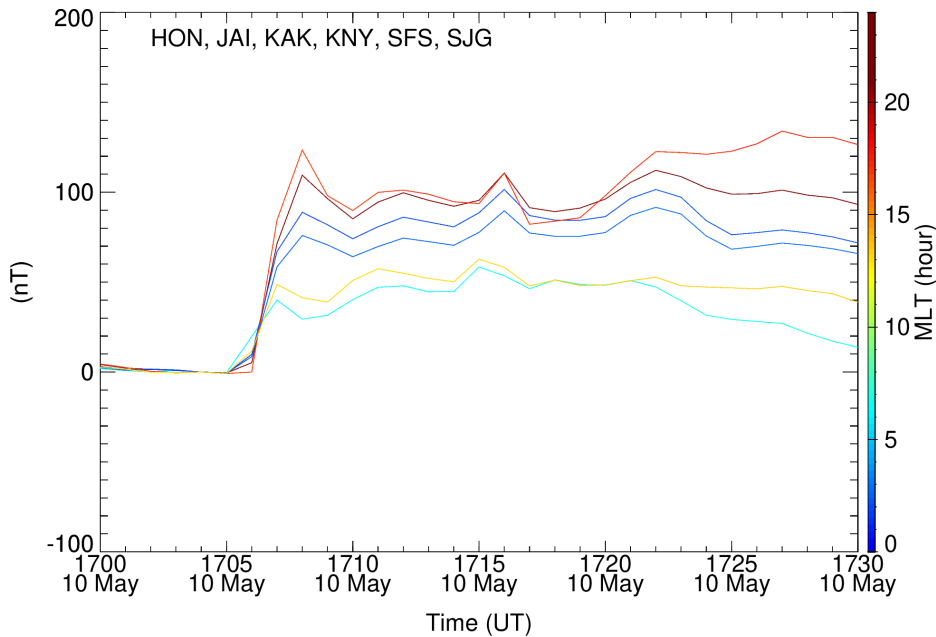


Figure 11: The north component (ΔX) of the geomagnetic disturbances at $20^\circ < \text{MLAT} < 30^\circ$. The colour codes indicate MLT (magnetic local time). The abbreviation codes indicate the sites used to plot.

Figure 12 summarises measurements of IMF and solar wind parameters, the SME index, the AL index, and the Dst index, and the absolute value of the magnetic latitude at which the aurorae and stable red auroral (SAR) arcs were reported. The IMF and solar wind parameters are acquired from the 5-min OMNI data (Papitashvili and King, 2020). We note that the IMF and the solar wind parameters were observed by the ACE spacecraft at $245 R_E$ upstream of the solar wind, and the data were time-shifted to the subsolar point of Earth's bow shock. Thus, the time-variations are not always correct due to ambiguity of the time-shifting algorithm, in particular, during the highly disturbed conditions. Because of this reason, we intend to overview the IMF and solar wind parameters briefly, not to go into detail. After the SSC (Figure 11), the geomagnetic storm showed a fast development and a monotonous recovery in terms of the temporal Dst evolution. The IMF B_z underwent fluctuations, reaching ≈ -40 nT around 18:05 UT. IMF B_z remained negative from 19:05 UT to 22:25 UT on 10 May. During this period, IMF B_z reached -40 nT. The IMF B_z turned positive, and turned negative again at 23:40 UT. During this northward IMF period, Dst recovered (increased) slightly. The southward IMF lasted by 04:35 UT on May 11. During this interval, Dst developed (decreased) again. The large amplitude southward component of the IMF caused a rapid decrease in the Dst index, that is the main phase of the storm. The real-time Dst index reached its minimum value of -412 nT at 2 UT on 11 May 2024, while the real-time Dxt reached a slightly lower minimum of 415.5 nT at the same time. This marks the end of the storm main phase and the storm

peak hour, to indicate a considerably fast storm development 474 nT and 479.8 nT in 9 hours in Dst index and Dxt index. According to Tsubouchi and Omura (2007), it is possible to calculate a statistical return period of geomagnetic storms of this magnitude (min Dst = -412 nT) as 5.7 years. The real-time Dst⁵/Dxt values are subject to small changes until definite values are established (WDC for Geomagnetism at Kyoto *et al.*, 2015; Karinen and Mursula, 2005; Mursula *et al.*, 2023).

Figure 12 shows that the Dst and Dxt indices follow each other quite closely, with momentary differences varying between -9nT and +6nT. Over the depicted time interval, the Dxt index is only slightly (less than 1 nT) lower than the Dst index. These differences are due to the somewhat different normalizations of the two indices (Karinen and Mursula, 2005; Mursula *et al.*, 2008; 2023).

The multiple complicated structures of ICMEs (Section 3) likely caused the two-step development of this storm. The intensification of the ring current was caused by the penetration of hot ions into the deep inner magnetosphere due to the dawn-dusk convection electric field intensified by the large amplitude southward IMF and fast solar wind. During the main phase of the storm, the solar wind speed was as high as $\approx 700\text{--}800$ km/s, and the southward component of the IMF was as high as ≈ 50 nT. The solar wind speed, maximum value of the southward component of the IMF, and minimum Dst index were similar to those of the large magnetic storm of 20–21 November 2003. The hot ions are speculated to penetrate as low as $L \approx 1.5$ to largely intensify the ring current (Ebihara *et al.*, 2005).

Figure 13 shows the local Dxt indices at the four Dst/Dxt stations. Their average makes the Dxt index. The largest compression at 17 UT on 10 May is observed at SJG (+93.9 nT) which is located at this time closest of all stations to noon, in the early afternoon of local time. The main phase development proceeds fairly similarly in all the four stations (at different local times) until 22 UT, after which somewhat larger differences start appearing. Note that only one station, HER⁶, reaches its local Dxt minimum at 2 UT, at the time of the (global) Dxt minimum, while SJG has it one hour before, HON two hours afterward at 4 UT and KAK only at 8 UT, six hours after the Dxt minimum.

At 2 UT on 11 May 2024, the real-time Dst increased, and the storm recovery phase began. During the recovery, the real-time Dst shows some negative excursions corresponding to the southward turning of the IMF Bz. Note that the local time of both KAK and HON at the time of their minimum observation is about 17 LT. For SJG it is 20 LT and for HER 3 LT. This is in agreement with the fact that, statistically, at low latitudes, the largest disturbance is found around 18 LT (Cummings, 1966; Yakovchouk *et al.*, 2012). This local-time dependence of the storm-time geomagnetic disturbances is often thought to be the partial ring current, but is probably not simple (Fukushima and Kamide, 1973). According to in-situ observations, the peak of the ring current takes place in the dusk-midnight sector (Terada *et al.*, 1998; Ebihara *et al.*, 2002; Le *et al.*, 2004). This is different from the ground-based magnetic observations. This discrepancy is probably attributed to the contribution from the field-aligned current (Ohtani *et al.*, 2007).

⁵ https://wdc.kugi.kyoto-u.ac.jp/dst_realtime/index.html

⁶ We are using station acronyms according to WDC for Geomagnetism at Kyoto (2020).

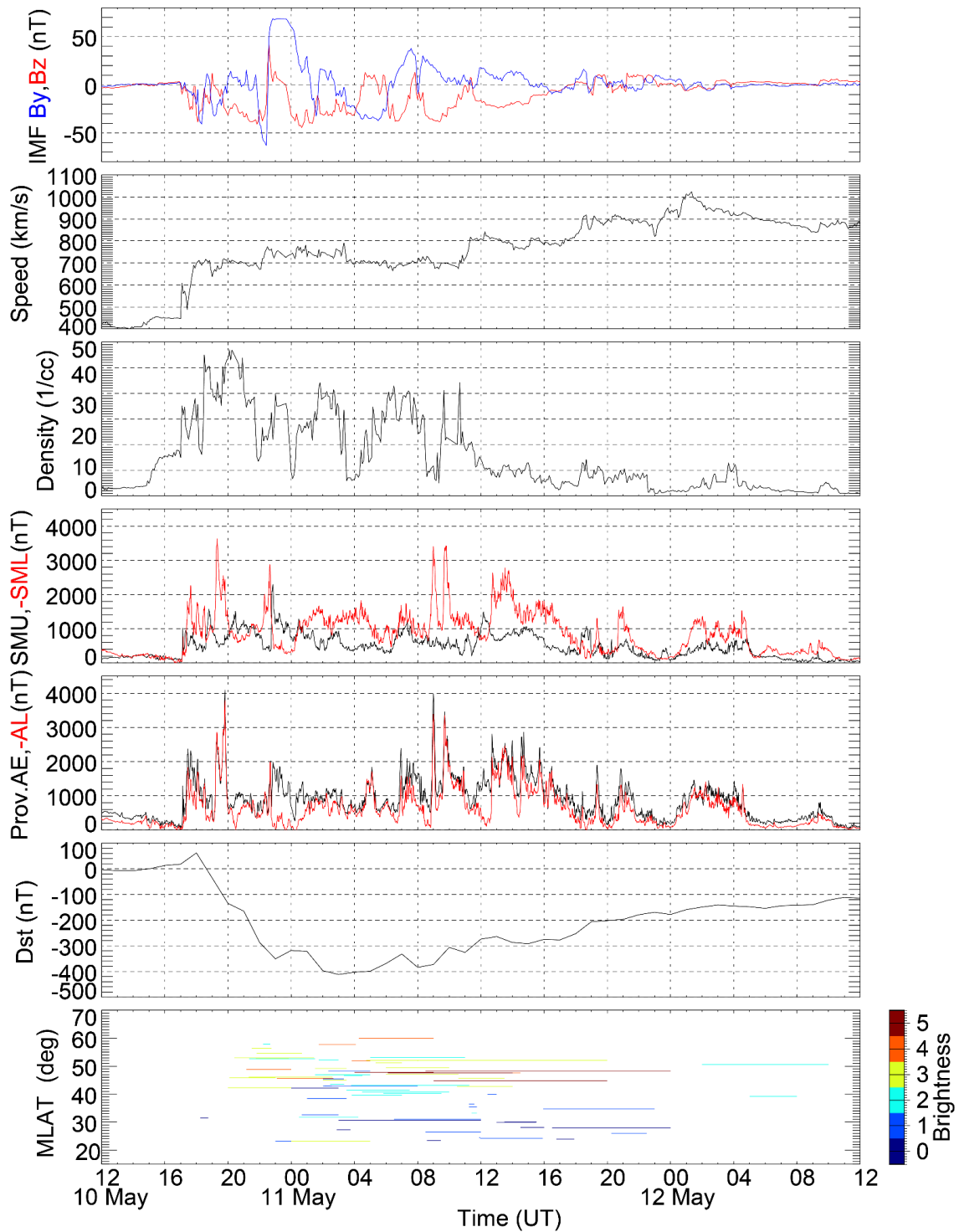


Figure 12: Temporal evolutions of interplanetary magnetic field (IMF), solar wind speed and density, geomagnetic disturbance, and auroral visibility. The first panel shows the interplanetary magnetic field of the solar wind in B_y (blue) and B_z (red) in the GSM coordinates. The second panel shows the solar wind velocity. The third panel shows the density of the solar wind. For these three panels, we have derived their source data from the 5-min OMNI data (Papitashvili and King, 2020). The IMF and the solar wind data are time-shifted to the subsolar point of Earth’s bow shock. Thus, the variations are subject to change depending on the algorithm of the calculation. The fourth panel

shows the SME (black) and SML (red) indices. The fifth panel shows provisional AE (black) and AL (red) indices. The sixth panel indicates the real-time Dst index. The last panel indicates the absolute value of the magnetic latitude at which the aurorae and SAR arcs were reported both by naked eye and instruments. The brightness is generally given with International Brightness Coefficient (IBC classification), apart from 0 for brightness not enough for naked-eye visibility and 5 for brightness more than full moon.

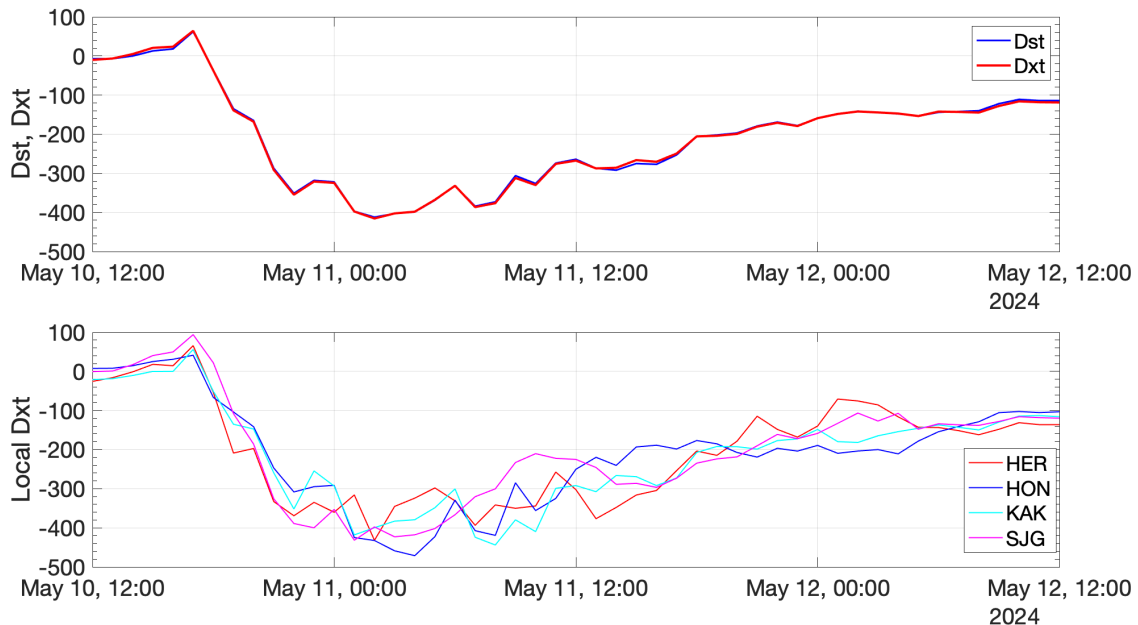


Figure 13: Comparisons of the Dst and Dxt indices in nT during the May 2024 storm. The lower panel shows *Dist H* of Hermanus (HER), Honolulu (HON), Kakioka (KAK), and San Juan (SJG).

As shown in Figure 12, the auroral electrojet has also developed significantly. The provisional AE and AL indices (WDC for Geomagnetism at Kyoto *et al.*, 2015b) initiated significant development at 17:06 UT on 10 May and increased to 2379 nT and -1830 nT, respectively, at 17:28 UT. These peak values were reached in 22 min. The abrupt jump in the provisional AE index is probably regarded as a shock-triggered substorm (Akasofu and Chao, 1980; Tsurutani and Zhou, 2003). The ionospheric current associated with the main impulse of the SC can also contribute to the abrupt jumps in these indices (Araki, 1994; Zhang *et al.*, 2023). During the storm's main phase, the provisional AE and AL indices reached peak values of 4098 and -3797 nT, respectively, at 19:48 UT on 10 May. Subsequently, these indices remained within $< |2000|$ nT during the main storm phase. During the storm recovery phase, these indices reached peak values of 3982 and -3797 nT at 09:00 UT on 11 May. According to a statistical study by Nakamura *et al.* (2015), up to 16 events occurred during which AL exceeded -3000 nT from 1996 to 2012, and the recurrence period for AL of -3797 nT was 1.49 years. In this sense, the provisional AL index of -3797 nT was not that extreme. We have to note that the AE and AL indices are not necessarily proportional to the intensity of the auroral electrojet. The auroral oval is suspected to have extended significantly equatorward from the AE stations during this interval, resulting in the suppression or saturation of the AE and indices. The SME index (Newell and Gjerloev, 2011) is used to overcome this issue since it is calculated from many sites, usually exceeding 100. The fourth panel of Figure 12 shows the SME index. Interestingly, the peak amplitude of the SML index, which is an extension of the AL index, is not always larger than that of the AL index. These values are provisional, so that the definitive conclusion cannot be obtained regarding the auroral electrojet.

Figure 14 summarises the north component of the geomagnetic disturbances ΔX at different latitudinal zones. The data was provided by INTERMAGNET (2021), and the sites used to plot are

summarised in Table 3. ΔX at 17:04 UT on 10 May 2024 is set to be zero. Diurnal variations, such as Sq, were not removed. Figure 14a shows ΔX at MLAT $> 75^\circ$. After the SSC, ΔX is negative on the duskside, whereas it is positive on the dawnside. The variations are reasonably explained by the twin vortices of the Hall current flowing in the ionosphere, known as the DP2 equivalent current (Nishida, 1968). In the poleward part of the DP2 current, it tends to flow westwardly on the duskside, and eastwardly on the dawnside as schematically illustrated at the right-bottom corner of Figure 14. The similar variations were also observed at high latitudes during the Carrington event in 1859 (Hayakawa *et al.*, 2019). Figure 14b shows ΔX in the latitudinal zone, $60^\circ < \text{MLAT} < 70^\circ$, which is usually referred to as the auroral zone. The lower envelope of ΔX in this panel is roughly equivalent to the AL index. The westward current is the most intense around midnight and in the postmidnight, which is consistent with the previous studies (*e.g.*, Kamide, 1982). In general, ΔX is positive on the duskside, and negative on the dawnside. This is consistent with the expectation that ΔX is primarily, not all, caused by the equatorward part of the DP2 current. Figure 14c shows ΔX in the lower latitudinal zone, $20^\circ < \text{MLAT} < 30^\circ$. The contribution from the ionospheric current is likely to be small. The contributions from the ring current, the tail current, the magnetopause current and the field-aligned current are probably significant. The averaged ΔX should be closed to the Dst index. During the main phase, the variations of ΔX show almost coherently with respect to MLT as mentioned above, but it is clearly shown that ΔX tends to be smaller on the duskside than on the dawnside. After the storm peak, the MLT dependence became significant. There are some negative peaks at ≈ 02 UT, ≈ 08 UT, and ≈ 14 UT on 11 May. These peaks took place in the pre-midnight sector, suggesting that they were primarily caused by the storm-time partial ring current. During the interval from ≈ 06 UT to ≈ 10 UT on 11 May, ΔX shows a negative excursion on the pre-midnight sector, whereas it shows a positive excursion in the pre-noon sector. This can be reasonably explained using the development of the partial ring current in the pre-midnight sector due to the injection of fresh ions from the nightside plasmashet, and the reduction of the ring current in the pre-noon sector due to the escape of the pre-existing ions in response to the rapid enhancement of the magnetospheric convection (Hashimoto *et al.*, 2002; Brandt *et al.*, 2002; Ebihara *et al.*, 2002).

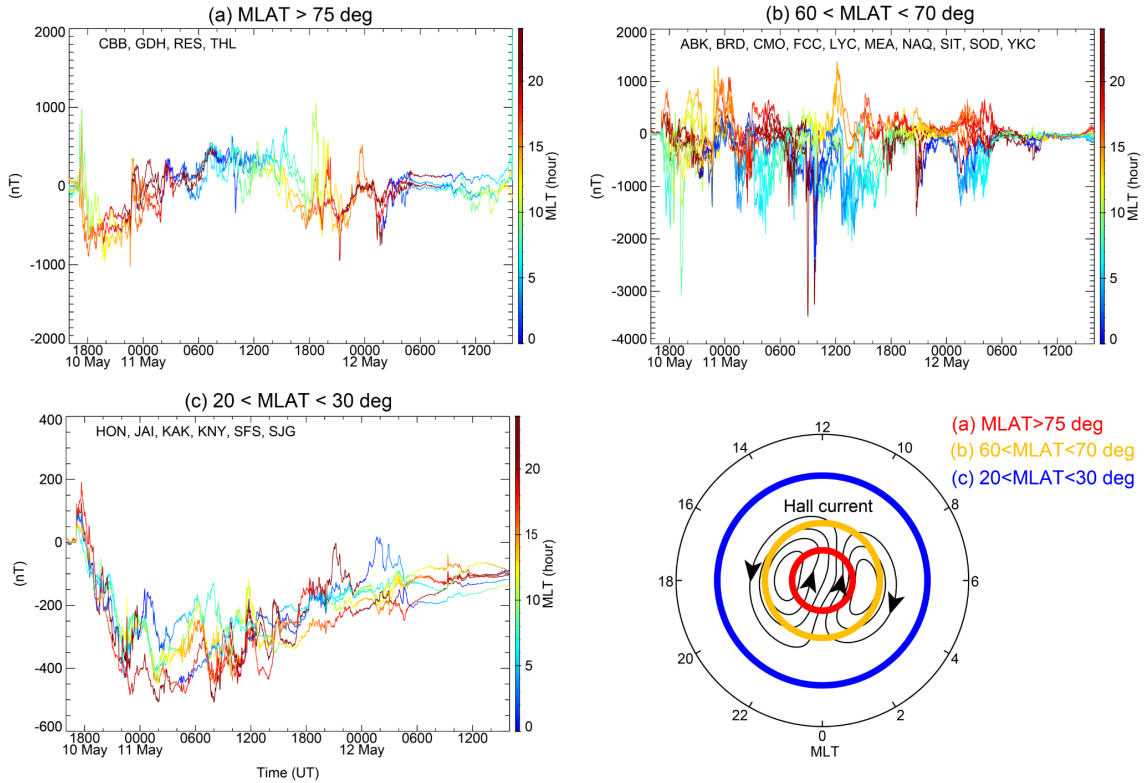


Figure 14: The north component of the geomagnetic disturbances ΔX at (a) MLAT $> 75^\circ$, (b) $60^\circ < \text{MLAT} < 70^\circ$ and (c) $20^\circ < \text{MLAT} < 30^\circ$, where MLAT stands for the magnetic latitude. The colour

codes indicate MLT. The abbreviation codes indicate the sites used to plot.

Table 3: Geomagnetic observatory sites used to plot Figure 14.

Abbreviation Code	Geographic Latitude (°)	Geographic Longitude (deg)
(a) MLAT > 75°		
CBB	69.12	254.97
GDH	69.25	306.47
RES	74.69	265.11
THL	77.47	290.77
(b) 60° < MLAT < 70°		
ABK	68.4	18.8
BRD	49.87	260.03
CMO	64.87	212.14
FCC	58.76	265.91
LYC	64.6	18.7
MEA	54.62	246.65
NAQ	61.16	314.56
SIT	57.06	224.68
SOD	67.4	26.6
YKC	62.48	245.52
(c) 20° < MLAT < 30°		
HON	21.32	202.0
JAI	26.92	75.8
KAK	36.23	140.19
KNY	31.42	130.88
SFS	36.7	354.1
SJG	18.11	293.85

7. Spatial Extents of the Auroral Visibility and the Auroral Oval: Naked Eye Observations

This storm significantly extended the auroral oval equatorward, as expected from the empirical correlation between the extension of the equatorward boundary of the auroral oval and the intensity of the associated geomagnetic storm (Yokoyama *et al.*, 1998; Blake *et al.*, 2020). As such auroral visibility was reported worldwide. We followed a citizen science approach to gather auroral visibility reports. This is a valid approach for reconstructing the equatorward boundary of auroral visibility and auroral oval, as reported by Case *et al.* (2016a). The authors prepared an online survey and called for auroral reports for the naked eye and instrumental visibility. This online inquiry allowed us to obtain 76 auroral reports, as exemplified with Figure 15. Figure 16 summarises responses from online survey responses. We located their geographic coordinates and computed their magnetic latitudes using the coordinates of the northern geomagnetic pole (N80.8 W72.6) in the IGRF-13 model (Alken *et al.*, 2021).

Figure 15: Examples of the reported auroral visibility throughout the world, from the top to the bottom [**NB: to appear in the record version**].

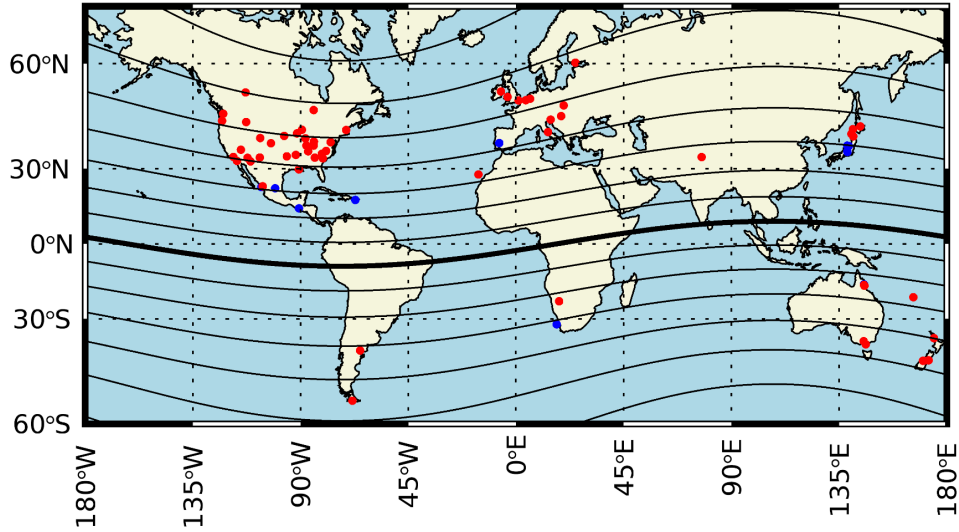


Figure 16: Geographical extents of the reported auroral visibility from 10 May 2024 to 12 May 2024. The contour lines indicate the magnetic latitude (MLAT) with an interval of each 10° . The solid line indicates the magnetic equator (0° MLAT). The red and blue dots indicated auroral report with naked-eye visibility and camera-visibility only, respectively.

On this basis, we confirmed the equatorward extent of naked-eye auroral visibility in both hemispheres. In the Southern Hemisphere, naked-eye auroral reports have been confirmed down to Boulouparis in New Caledonia ($S21^\circ54'$, $E165^\circ59'$, -26.5° MLAT), Chewko Lookout in Australia ($S17^\circ03'$, $E145^\circ22'$, -24.2° MLAT), and Tivoli Astrofarm in Namibia ($S23^\circ28'$, $E018^\circ01'$, -23.2° MLAT). In the Northern Hemisphere, naked-eye auroral reports have been confirmed down to El Peyote ($N22^\circ41'$, $W100^\circ36'$, 30.7° MLAT) and Leh in India ($N34^\circ10'$, $E077^\circ33'$, 26.1° MLAT).

Auroral visibility at any site did not immediately indicate overhead auroral visibility. Therefore, we must reconstruct the equatorward boundaries of the auroral oval (EBAO) considering the MLAT and the reported altitude at each site. The altitude profiles were used to reconstruct the EBAO conservatively. We assumed the altitude of the visual aurorae to be approximately 400 km, following Roach *et al.* (1960) and Ebihara *et al.* (2017), to keep consistency with the previous estimates for the historical storms (Miyake *et al.*, 2019; Usoskin *et al.*, 2023). We quantified the equatorward boundaries of the auroral emission regions by measuring their invariant latitude (ILAT) and tracing the footprints of the magnetic field lines where the auroral electrons precipitated, McIlwain *et al.* (1961).

In the Southern Hemisphere, we have reconstructed the EBAOs down to 29.8° ILAT based on a Namibian report from Tivoli Astrofarm ($S23^\circ28'$, $E018^\circ01'$, -23.2° MLAT) with a naked eye auroral visibility up to 45° . This is somewhat followed by the Australian report from Bromfield Swamp ($S17^\circ22'$, $E145^\circ33'$, -24.5° MLAT) with a naked eye auroral visibility up to 20° and the New Caledonian report from Boulouparis (-26.5° MLAT) with a naked-eye auroral visibility of up to 20° that allow the reconstruction of the equatorward boundaries of the auroral oval (EBAO) down to 35.0° ILAT and 36.7° ILAT, respectively. In the Northern Hemisphere, a Mexican report from Chirimoyos ($N23^\circ26'$, $W105^\circ48'$, 31.0° MLAT) allowed us to reconstruct the EBAO down to 35.5° ILAT based on the reported naked-eye auroral altitude of 60° . This is slightly more equatorward than what we can reconstruct from another Mexican report from El Peyote ($N22^\circ41'$, $W100^\circ36'$, 30.7° ILAT) with a reported naked-eye auroral altitude of 25° . Overall, our reconstructions in both hemispheres were reasonably consistent: 29.8° ILAT in the Southern Hemisphere and 35.5° ILAT in the Northern Hemisphere.

Caveats must be noted on these estimates because SAR arcs often reach farther towards the magnetic equator from the auroral ovals. The SAR arcs appear monochromatically in reddish colouration, in contrast to the actual reddish auroral emissions (Kozyra *et al.*, 1997; Shiokawa *et al.*, 1997). Therefore, we need to choose records with non-reddish colours or explicit structures to rule out SAR arcs and conservatively reconstruct the EBAO to be free from contamination of SAR arcs. The reports that we used to reconstruct the EBAOs in both hemispheres included non-reddish colourations (pinkish and purplish components in Bromfield in Australia, and pinkish components in Chirimoyos in Mexico) and explicit structures (in Chirimoyos, Mexico and Tivoli Astrofarm in Namibia). Mendillo *et al.* (2016) reported that patches of emission at the oxygen green line (557.7 nm) are superimposed to the SAR arcs. After considering the possibility that precipitating ions gave rise to the oxygen red line, Rees and Deehr (1961) suggested that precipitation of low energy electrons could result in the emission at the oxygen green line, together with head conduction from the plasmopause-ring current interaction region, which could result in the SAR arcs. For now, we cannot exclude the possibility that the monochromatic reddish aurora witnessed at low latitudes was associated with the SAR arcs, as was also the case with historical auroral reports.

8. Spatial Extents of the Auroral Visibility and the Auroral Oval: Instrumental Observations

In contrast, the auroral visibility and auroral oval were captured further equatorward by camera observations, most probably because of the different detection thresholds of naked eye observations and optical instruments, such as cameras. Good examples can be easily obtained from Japanese cases. The aurora was photographed at least down to Koumi (N36°04', E138°24', 28.1° MLAT). More photographs on social media show auroral visibility at lower latitudes, but they require further careful validation (*e.g.*, Meel and Vishwakarma, 2020). In contrast, the naked eye visibility is confirmed only down to Hiranai (N41°01', E140°53', 33.2° MLAT). The Hiranai report showed striking differences in the spatial auroral extents: by the naked eye, up to 20° in elevation, and by optical instruments, up to 70° in elevation. Following the procedure described in Section 7, this study allowed us to reconstruct the equatorward boundary of the auroral oval at Hiranai, down to 43.0° ILAT and 36.8° ILAT, for the naked-eye-based and camera-based estimates, respectively. The equatorward boundary looks significantly decent in contrast to our reconstructions in Section 6, as Japanese observers were under broad daylight around the storm peak (≈ 2 UT), only managed to see the storm recovery phase, and probably missed the most dramatic part of the auroral display.

Figure 17: Examples of auroral photographs from Japan, from the top to the bottom [**NB: to appear in the record version**]

Similar cases have been reported throughout the world. An Indian auroral report from Leh in India (N34°10', E077°33', 26.1° MLAT) described the auroral altitude therein as 5° by the naked-eye and 10° by camera. Similarly, the New Caledonian report from Boulouparis described auroral altitude as 20° by the naked eye and 30° by a camera. This difference varies the EBAO to 36.7° ILAT (by the naked eye) and 34.5° ILAT (by the camera). At Tivoli Astrofarm in Namibia (S23°28', E018°01', -23.2° MLAT), aurora was confirmed up to 45° by the naked eye and up to 55° by the camera. Subsequently, its internal structure was confirmed to be up to 20° by photographic analysis (Figure 15). Notably, these examples occurred at different times during the storm, as shown in Figure 16.

Overall, in the Northern Hemisphere, the aurora was photographed at least down to San Juan Sacatepéquez in Guatemala (N14°43', W090°39', 23.4° MLAT) subvisually without naked eye visibility. In the Southern Hemisphere, the aurora was photographed at least down to Big Mitchell Reserve in Australia (S16°48', E145°21', -23.0° MLAT). From these cases, it is evident that the naked eye visibility is significantly different from instrumental detectability. The instrumental detectability should be of course somewhat variable up to the instrumental set ups such as exposure time.

The equatorward extent of the visibility with camera is different from that with naked eyes. This

discrepancy is primarily attributed to the different sensitivity. The sensitivity of the camera is much higher than that of naked eyes. We could suggest three possible scenarios for its provenance as detectability difference in (1) vertical extents, (2) latitudinal extents, or (3) their combinations. For Scenario (1), the aurora at high altitudes could have been detected only by the cameras, so that the aurora was visible at lower latitudes. For this scenario, the equatorward boundary is assumed to be the same. For Scenario (2), the equatorwardmost boundary of the auroral oval was fairly broad in latitude, and the aurora extended further equatorward diffusively. According to the DMSP satellite observations, the equatorward boundary of the electron precipitation is broad in latitude during large magnetic storms (Shiokawa *et al.*, 1997; Ebihara *et al.*, 2017). Precipitations of electrons with low energy and low flux could cause auroral emission further equatorward, but the auroral emission could be too dim to be visible to the naked eye observations. For this scenario, the altitude distribution of the aurora is assumed to be the same. It is of course possible that both were the case, as expected in Scenario (3). Further quantitative assessments are needed here.

For the moment, we accommodate as wide error margins as possible. It is empirically known that the maximum brightness of the reddish component of the aurora (at 630.0 nm) is located around 220 km in altitude, and it can range from 200 to 300 km (Solomon *et al.*, 1988). On the basis of spectra of precipitating electrons observed at mid latitudes near the storm maximum of the large magnetic storm of 13-14 March 1989, the volume emission rate of 630.0 nm peaks at about 270 km altitudes (Ebihara *et al.*, 2017). At 400 km altitude, the volume emission rate of 630.0 nm is an order of magnitude lower than that at the peak altitude. At 500 km altitude, the volume emission rate is much lower than that at the peak altitude. From this consideration, we set the altitudes of the upper limit of the aurora identified by camera to be 300, 400, 500, and 800 km. In this case, the Namibian report from Tivoli Astrofarm (-23.2° MLAT), which has a local altitude with instrumental detectability of 55° above the local horizon, allows us to derive the EBAO as, at least, 27.6° , 28.9° , 30.1° , and 33.3° ILAT, respectively. Alternatively, the Australian report from Big Mitchell Reserve (-16.8° MLAT), which has a local altitude with instrumental detectability of 50° above the local horizon, allows us to derive the EBAO as 22.4° , 24.0° , 25.4° , and 29.1° ILAT, respectively. Further detailed assessments are needed with parallel case studies.

9. Spatial distribution of the Auroral Activity

Figure 16 shows a graphical summary of the temporal and spatial evolution of auroral visibility during the May 2024 storm, showing variations in the maximum auroral brightness. Based on the real-time Dst index, the auroral visibility below $|40|^\circ$ MLAT was concentrated in the late main phase and early recovery phase of this storm. One interesting account is a subvisual auroral observation from a ship in the South Atlantic Ocean ($S32^\circ00'$, $E17^\circ00'$, 31.5° MLAT) that lasted from 18:15 to 18:45 UT on 10 May. This aurora was photographed shortly after a SSC, despite its occurrence at lower latitudes. A similar case was observed during the March 1989 storm (Boteler *et al.*, 2019).

This figure also shows the temporal and spatial evolution of the maximum auroral brightness at each site. We gathered and compared citizen contributors' self classification and descriptions on the maximum brightness in total illumination with an IBC reference (Chamberlain, 1961, p. 124) with an extension: (0) not visible by the naked eye; (1) Comparable to Milky Way; (2) comparable to thin moonlit cirrus clouds; (3) comparable to moonlit cumulus clouds; comparable to the full moon; and (4) brighter than any such references. This figure shows that the maximum brightness was higher in higher latitudes and lower at lower latitudes. This, in turn, shows gradual decreases in auroral brightness in lower MLATs and partially explains the smaller geographical extent of the naked-eye auroral visibility than that by instrumental observations.

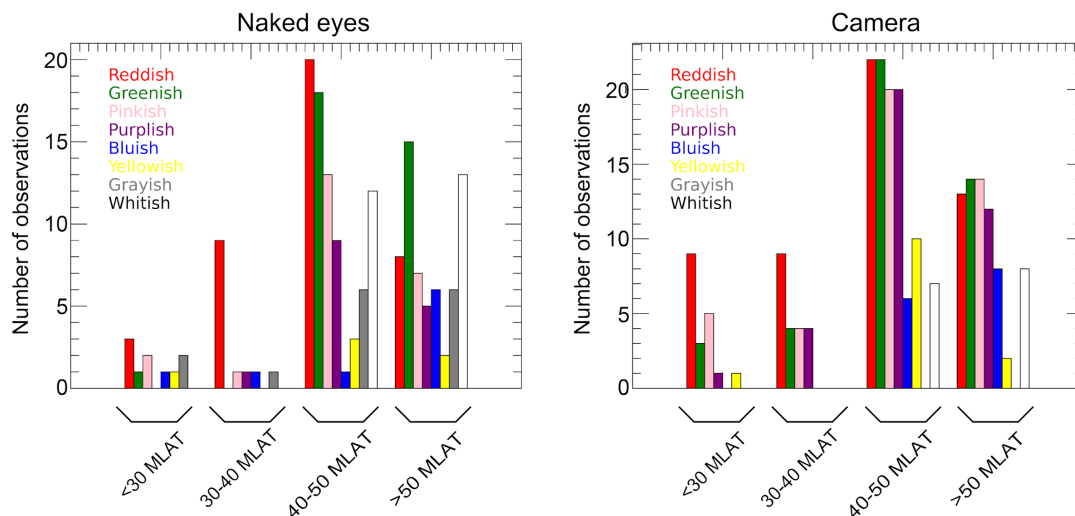


Figure 18: Amounts of reported auroral colourations in each MLAT ranges by naked eye (left) and by camera (right), showing (1) $< 30^\circ$ MLAT, (2) $30^\circ - 40^\circ$ MLAT, (3) $40^\circ - 50^\circ$ MLAT, and (4) $> 50^\circ$ MLAT, from left to right.

Figure 17 shows the number of auroral colourations reported in each MLAT range by the naked eye and the camera. A considerable number of reports show reddish and greenish colouration. These colours are typically associated with oxygen emissions at 630.0 nm (reddish) and 557.7 nm (greenish), owing to the precipitation of electrons. Reddish aurorae can more easily be seen than green aurorae by camera. Greenish aurorae cannot be spotted by eye as far south, generally because they occur at lower altitude. The yellowish colour is most likely caused by a mixture of reddish and greenish colours. The number of reports with greenish colouration was comparable to that with reddish colouration at $> 40^\circ$ MLATs, whereas it significantly decreased below 40° MLAT by naked eye observation. For camera observations, a greenish colouration was reported below 40° MLAT. Purplish and pinkish colours have also been reported below 40° MLAT. They are typically associated with nitrogen emissions, including 427.8 nm for N_2^+ . Although bands of N_2^+ are known to coexist in the reddish auroral arc (Rees and Deehr, 1961), this may challenge the conventional wisdom that a low-latitude aurora is dominated by a reddish colour. For the purplish auroras that appear at high altitudes, the energy of the precipitating electrons is not necessarily high. The purplish aurora appeared to be dominant over the reddish one in some of the pictures, as exemplified with Víctor R. Ruiz's photograph in Mogán of Gran Canaria (Figure 15). The dominance of the purplish aurorae should be investigated in future studies, including different response bands of cameras and cell phones. It should be noted that greenish colouration should have been seen in different colours, such as grayish, by naked eye observation.

10. Temporal and spatial variation of electron density (total electron content) in the ionosphere

In previous sections, we showed the characteristics of temporal and spatial variation of geomagnetic field, ionospheric convection, and auroral oval during the geomagnetic storm. Considering the magnitude of geomagnetic field perturbations and ionospheric convection, it can be expected that a large amount of electromagnetic energy input from the magnetosphere to the ionosphere produces a severe positive and negative storms which show an increase and decrease of electron density in the ionosphere. To confirm these signatures in the ionosphere during the geomagnetic storm, we analysed global total electron content (TEC) data with high spatial resolution of $0.5^\circ \times 0.5^\circ$ in geographic latitude and longitude.

Figure 19 shows the polar map of the ratio of the TEC difference (rTEC) (Shinbori *et al.*, 2019) in the Northern Hemisphere in altitude adjustment corrected geomagnetic (AACGM) coordinates

(Section 4.2 of Laundal and Richmond (2017)) at 17:00 UT and 22:00 UT on 10 May and 18:00 on 11 May corresponding to the pre-storm phase, main and recovery phases of the geomagnetic storms, respectively. During the pre-storm phase, the rTEC value was almost zero in the entire region except for the west coast of North America in an MLAT range from 50° to 70° . This means that the spatial distribution of rTEC is geomagnetically at a quiet level. During the main phase, the characteristic structure of rTEC appeared from the high- to low-latitude regions. A large enhancement of rTEC with a value of more than 1.0 occurred in the low latitudes (20° – 50° MLAT) of the dusk sector (13–20 h MLT). This structure corresponds to a storm-enhanced density (SED) (Foster, 1993). Further, the SED connects a spatially narrow enhancement of rTEC extending from the dayside to nightside in the polar region. This phenomenon has been called a tongue of ionisation (TOI), which is caused by plasma transportation from the dayside mid-latitude ionosphere into the polar cap due to enhanced convection electric fields during the main phase of geomagnetic storms (David *et al.*, 2011; Foster, 1989, 1993). Shinbori *et al.* (2022) showed a seasonal dependence of the amplitude of SED and TOI as a function of the magnitude of geomagnetic storms. According to their statistical analysis result, the amplitude of SED and TOI becomes maximum in winter and minimum in summer. However, in spite of the summer season when most of the polar regions are sunlit in the Northern Hemisphere, the large enhancement of rTEC related to the occurrence of SED and TOI was observed during the geomagnetic storm on 10/11 May 2024. The occurrence feature is different from what previous studies have reported. This implies that an intense convection electric field is imposed on the ionosphere from the high to low latitudes during this geomagnetic storm event. On the other hand, a narrow-banded enhancement of rTEC appeared in an MLAT range of 45° – 55° in the nightside (22–03 h MLT). This rTEC enhancement corresponds to extension of the auroral oval. This result implies that the auroral oval extended to the lower latitudes as shown in the previous section. Equatorward of the rTEC enhancement, a decreased rTEC region appeared with a narrow-banded structure in an MLAT range of 25° – 45° . The rTEC depletion is a mid-latitude trough corresponding to the location of the plasmopause in the inner magnetosphere (*e.g.*, Shinbori *et al.*, 2019). During the recovery phase, the spatial distribution of rTEC globally shows a large decrease in the entire region from the high to low latitudes. The value reaches -0.75 on the dayside. The rTEC depletion corresponds to a negative storm which is caused by a decreasing electron density in the ionosphere due to the enhancement of the recombination process associated with an increasing N_2 density. This result suggests that the large depletion of the electron density in the ionosphere severely influences the propagation property of electromagnetic waves used in satellite navigation and positioning.

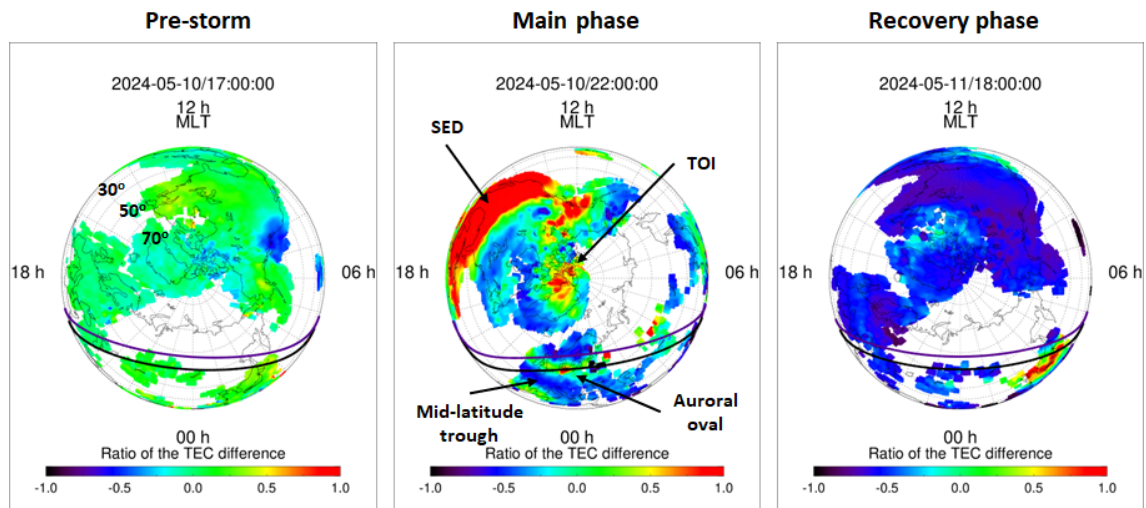


Figure 19: Polar map of ratio of the TEC difference (rTEC) in the Northern Hemisphere in altitude adjustment corrected geomagnetic (AACGM) coordinates during the pre-storm, main phase, and recovery phase. The colour bar in each panel indicates the rTEC value in a range of -1.0 to 1.0 . The black and purple curves show the sunset terminators at an altitude of 105 and 300 km, respectively.

11. Summary and Discussions

In this article, we have reviewed the data of the May 2024 solar and geomagnetic storms as a flash report. The source AR 13664 rapidly increased the area from 113 MSH to 2761 MSH from 1 May to 9 May (Figures 1 and 2). This rapid growth also increased the total energy of the nonlinear force-free field, the potential magnetic field, and the free magnetic energy especially from 7 May to accommodate 12 X-class flares between 8 and 15 May, even up to X8.7 (Table 1 and Figure 2).

This AR is associated with at least 10 halo CMEs. Their velocity measurements allow us to associate the CME launched at 22:24 on 8 May 2024 with the extreme geomagnetic storm that started from SSC at 17:05 on 10 May (Figure 4). This indicates a propagation time of the ICME as 42 h 41 m. This ICME collided and piled up with at least three preceding ICMEs before arriving at the Earth. The IPS responses were detected in a large amplitude. These signals are associated with the high-density region where the fast-propagating ICMEs pile up the background solar wind and might support the ICME-ICME interaction in the interplanetary space.

One of these solar eruptions triggered a Forbush decrease in CRs and solar proton event. The ICMEs caused a relatively large Forbush Decrease of $\geq 15\%$ in the maximum decrease in the NM count rate. Subsequently, both the polar NMs and GOES-16 satellite register a notable CR increase around 2–3 UT (Figure 6). This increase is confirmed as a GLE and included in the International GLE Database as GLE #74.

The ICME arrivals considerably compressed the magnetosphere. THEMIS spacecraft measurements allow us to confirm crossings of THEMIS spacecraft over the boundary of the magnetosphere at $\approx 8.24 R_E$ at 17:05 UT (Figure 7), $\approx 8.51 R_E$ at 17:05 UT (Figure 8), $\approx 5.04 R_E$ at 19:12 UT (Figure 9), $\approx 5.37 R_E$ at 19:19 UT (Figure 10). Particularly for THEMIS-E and THEMIS-A at 1912 UT and 1919 UT, observations indicate that the magnetopause underwent an extreme inward motion going beyond the geosynchronous orbit ($6.6 R_E$) which takes place during intense substorms occurring under high magnetospheric compressions (Oliveira *et al.*, 2021). Major loss processes for radiation belt particles occur during such extreme events (e.g., Turner *et al.*, 2012). Those extreme events have profound space weather implications to satellites in geospace because satellites can be exposed to energetic radiation belt particles that may partially or totally damage their electronic systems (Hands *et al.*, 2018). For example, if the satellite re-enters the magnetosphere and the radiation belts when the magnetopause moves back outward, the likelihood of damage occurrence is amplified if there is an increase in energetic particle injections associated with rapid energetic particle injections and wave-particle interactions (Baker *et al.*, 2017; Koons & Fennell, 2006). Therefore, satellites in geospace may have been exposed to harsh space weather conditions during the 10 May 2024 extreme geomagnetic storm.

Upon shock arrival, the SSC took place at 17:05 UT in multiple observatories such as Kakioka (≈ 78 nT) and San Fernando (≈ 130 nT), showing local enhancements in the duskside especially in the summer hemisphere. This LT effect probably enhanced the SSCs in the European sector.

The resultant geomagnetic storm developed to min Dst = -412 nT and min Dxt = -421.8 nT at 2 UT on 11 May. The auroral electrojet has been intensified up to 4098 nT in the provisional AE index and -3797 nT in the provisional AL index in the main phase and 3982 nT in the provisional AE index and -3797 nT in the provisional AL index in the recovery phase. In between, the provisional AE and AL indices reduced intensity, probably because the auroral oval went further equatorward and stayed away from the AE/AL observatories. However, we should not exaggerate their magnitudes, as the statistical studies indicate the return periods as 5.7 years in Dst index (Tsubouchi and Omura, 2007) and 1.49 years in AE index (Nakamura *et al.*, 2015). Perhaps, the geomagnetic activity in SC 24 was considerably quieter than normal SCs.

The DP2 ionospheric current was significantly enhanced (Figure 14). This enhancement manifests

the intensification of the magnetospheric convection. The intensified magnetospheric convection is highly likely to cause the earthward penetration of the hot plasma originating in the plasma sheet so as to enhance the ring current.

This storm also caused considerable disturbances in the ionosphere (Figure 19). This storm left a storm-enhanced density in the ionosphere, showing large rTEC in the lower MLATs ($20^\circ - 50^\circ$) in the duskside (13 – 20 MLT) and tongues of ionosphere extending from the dayside to the nightside in the polar region, despite unfavourable seasonality in the Northern Hemisphere. This indicates an imposition of the intense convection electric field on the high to low MLATs in the ionosphere. These TEC records also confirmed rTEC enhancements in a narrow-band in $45^\circ - 55^\circ$ MLAT in the nightside, confirming equatorward extension of the auroral oval in accordance with the visual auroral records. The rTEC also showed plasmopause in the inner magnetosphere with a depletion in the $25^\circ - 45^\circ$ MLAT. During the recovery phase, the rTEC globally showed a considerable negative storm.

Within space age (from 1957 onwards), this storm magnitude of $\text{min Dst} = -412$ nT is comparable to four of the five greatest geomagnetic storms in space age, namely those in Sep 1957 ($\text{min Dst} = -427$ nT), February 1958 ($\text{min Dst} = -426$ nT), July 1959 ($\text{min Dst} = -429$ nT), and November 2003 ($\text{min Dst} = -422$ nT), and surpassed significantly only by the extreme storm in Mar 1989 (WDC for Geomagnetism at Kyoto *et al.*, 2015; Riley *et al.*, 2018). This value should be revised in the future, as this real-time Dst index was developed using a different method from the final Dst index⁷, extending only to 2016 at the time of writing. In the Kp index (Matzka *et al.*, 2021), this geomagnetic storm recorded the greatest value (Kp = 9) after October 2003 (Yamazaki *et al.*, 2024). This geomagnetic storm is also the second to the fifth greatest in the Hp30 index since 1985 (Yamazaki *et al.*, 2024). In this regard, this geomagnetic storm was certainly large but not unique.

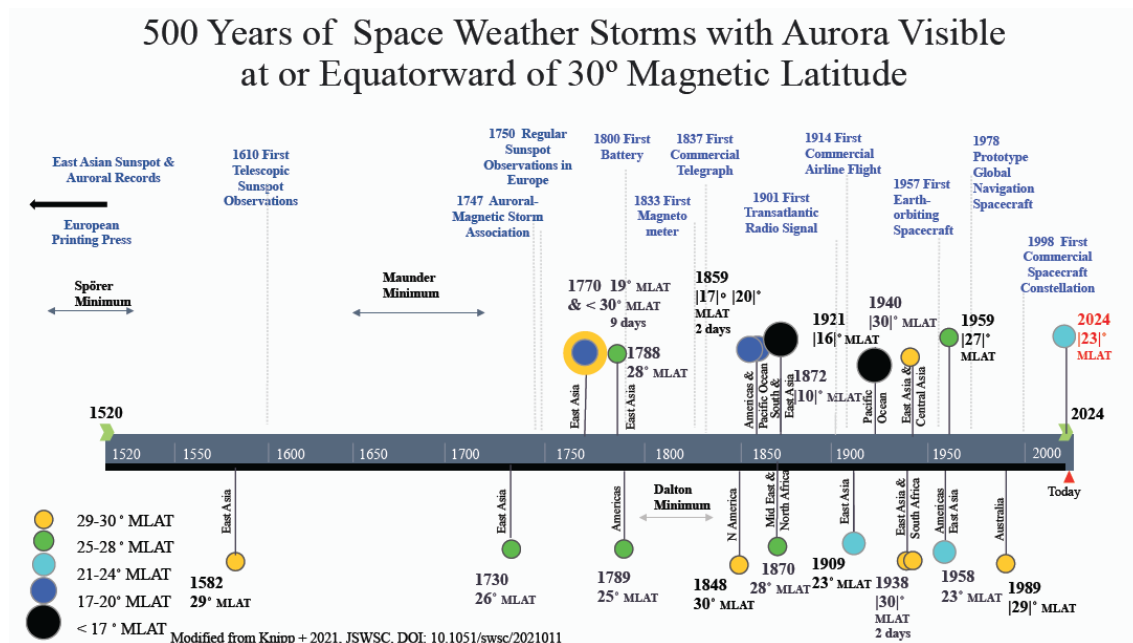


Figure 20: The spatial extents of naked eye auroral visibility upon extreme geomagnetic storms in history with the auroral visibility reported $< |30|^\circ$ MLAT, as modified from Knipp *et al.* (2021) and Hayakawa *et al.* (2024).

During this storm, the auroral display was visible down to $|23.2|^\circ$ MLAT (Tivoli Astrofarm in Namibia) by the naked eye (Figure 15). This allows us to reconstruct the EBAO down to 29.8° ILAT.

⁷ https://wdc.kugi.kyoto-u.ac.jp/dst_final/index.html

Figure 20 contextualises this storm with auroral visibility in historical storms, as modified by Knipp *et al.* (2021) and Hayakawa *et al.* (2024). Based on naked eye observations, this storm is comparable to the extreme storms in February 1958 (down to $|23.3|^\circ$ MLAT) and July 1959 (down to $|27.4|^\circ$ MLAT). In contrast, camera observations showed visibility at even lower latitudes, indicating that this storm was even potentially comparable to the Carrington storm in 1859. However, caveats must be noted here: aurorae in most historical space weather events were recorded not by the camera but by the naked eye, especially in the lower MLAT regions. The earliest datable auroral photograph in Japan was taken in 1958 (Hayakawa *et al.*, 2023a). Therefore, comparing naked-eye observations of the May 2024 storm with auroral visibility during historical extreme storms is appropriate.

Moreover, the space weather forecasts and real-time news releases motivated a number of the observers to come out to seek for aurorae. One of the observers in Far North Queensland “drove approximately 350 km throughout the night” and changed the observational site three times to minimise disturbances from the rain, and light pollution (Figure 15). Journalists of Hokkaido Newspaper saw the space weather forecasts and worldwide news pieces and decided to direct cameras to the northern sky. At least two Japanese astrophotographers saw space weather forecasts to take a flight and drive to photograph auroral activity in a remote site without significant light pollution. They are not what happened upon the past extreme geomagnetic storms such as those in 1957, 1958, and 1959 (Hayakawa *et al.*, 2023a, 2024). The Aurorasaurus platform automatically generates alerts based upon the predicted auroral oval visibility as well as reports from clusters of citizen scientists on the ground, which may be further equatorward of the predicted oval (Case *et al.*, 2016b). These latter alerts were generated in Texas and Florida for this extreme storm⁸.

These naked eye observations are especially important for comparison of the modern storms with historical storms to have the same threshold, as the human eye and camera have different sensitivity thresholds, which has challenged the comparison of modern storms based on instrumental auroral data and past extreme storms based on historical visual auroral reports.

This storm is probably one of the earliest extreme auroral storms captured primarily with digital cameras and smartphones. The response of smartphones to the auroral visibility, with automatic noise reduction, has not been well quantified and requires further investigations on their potential variations. Our case studies have evidently confirmed that the cameras can detect aurorae in lower latitudes than naked eye observers (Figure 17). This is also confirmed with the Japanese camera observations that captured aurorae much more frequently than the naked-eye observations (*e.g.*, Miyaoka *et al.*, 1990; Shiokawa *et al.*, 2005). Therefore, it is secure to consider the EBAO extending more equatorward than what we can reconstruct for naked-eye observations. The satellite observations have shown some cases where the equatorward boundary of the auroral electron precipitation to be somewhat fuzzy and indefinite (*e.g.*, Newell *et al.*, 1996; Ohtani *et al.*, 2010). For these cases, these satellite measurements might have seen ion precipitations (Rees, 1961; Lummerzheim *et al.*, 2001) or SAR arcs (Kozyra *et al.*, 1997). Owing to this difficulty, it is not readily evident what the EBAOs estimated from naked-eye observations and camera observations are seeing within the distributions of electron precipitation. We need future analyses for this problem comparing satellite data for particle precipitations and ground-based observations by naked eye and camera. Therefore, we have to set a caveat that the EBAO is no more than a preliminary estimate.

Historical records indicate that the equatorward boundary of auroral ovals extends down to $33 - 40^\circ$ ILAT during the greatest geomagnetic storms in the space age (Boteler, 2019; Hayakawa *et al.*, 2023a, 2024) and down to $24 - 25^\circ$ in historical extremes (Hayakawa *et al.*, 2020, 2023b). Analysing modern naked eye observations and comparing them with historical cases is important to better contextualise extreme storms.

However, our reconstruction was most likely an ultra-conservative estimate. The scientific

⁸ <https://science.nasa.gov/science-research/heliophysics/aurorasaurus-roars-during-historic-solar-storm/>

community has hosted large-scale citizen science portals, such as Aurorasaurus⁹ (Macdonald *et al.*, 2015; Kosar *et al.*, 2018a), which can significantly increase the number of auroral records. The utility of their citizen science datasets have been already confirmed for ground-truth on satellite observations and boundary estimations for a case study on the intense geomagnetic storm in March 2015 (Kosar *et al.*, 2018b). In the near future, we need to call for detailed reports from individual contributors to document the temporal evolution, spatial evolution, and colouration of the reported auroral displays. These details allow us to improve the reconstruction of auroral emissions, their temporal/spatial evolutions, and the equatorward boundary of the auroral oval. Moreover, because this occurred in mid-May, the European and North American sectors had the disadvantage of longer daytime durations with better weather conditions in Europe and the US. The storm peak chronologically suggests favourable auroral visibility conditions in the Southern Hemisphere, particularly in South America. We need to call for the recollection of this visual aurora by citizens, especially individual astronomers, in multiple languages. As well, outreach efforts to explain the scientific phenomena in plain language are important to include and empower the public, as exemplified with the Aurorasaurus blog¹⁰.

At that time, auroral photographs were being uploaded from a large part of the world. This significant geographical extent can be partially explained by the difference in the sensitivities of naked eye observers and cameras. We have significantly better access to optical instruments, such as cameras, than past space weather events. Moreover, space weather forecasts have allowed and motivated people to see the aurora at the right moment. They even directed the camera to the sky to determine whether they could capture aurorae. Several observers confirmed these cases. Furthermore, the internet/SNS accessibility allows observers to swiftly exchange reports/photos. This has motivated more people to hunt for auroral visibility. At the same time, we have difficulty with the light pollution of the night sky that made auroral visibility from the urban areas more difficult (Smith, 2008; Falchi *et al.*, 2016). Therefore, we have three favourable aspects and one negative aspect for the coverage of auroral photographs and auroral observers than auroral extensions during historical extreme geomagnetic storms.

This is no more than a flash report with provisional datasets. We definitely need to accumulate more precise datasets and compare them with modelling results. With further analyses, this solar and geomagnetic storm may allow us to bridge our modern scientific knowledge to the extreme solar and geomagnetic storms recorded in the past and better assess the extremes of space weather.

Data Availability

We have acquired sunspot number and sunspot drawings from the SILSO and USET of the Royal Observatory of Belgium, the solar wind parameters and proton and X-ray fluence from the NOAA, the IPS data used from the ISEE, Nagoya University website <https://stsw1.isee.nagoya-u.ac.jp/vlist/>, neutron monitor data from the International GLE database, and geomagnetic Dst, AE, and AL indices from WDC and the location of north geomagnetic pole for Geomagnetism at Kyoto. We also acknowledge the Oulu Cosmic-Ray Station, the Neutron Monitor Database and individual NM station managers for maintaining the cosmic-ray measurement datasets over a long time period. The TEC data are available on the ISEE, Nagoya University website <https://stdb2.isee.nagoya-u.ac.jp/GPS/GPS-TEC/>. We thank Samuel Freeland for offering Event Archives of Solar Soft in the Lockheed Martin Solar & Astrophysics Laboratory.

Acknowledgments

This research was conducted under the financial support of JSPS Grant-in-Aids JP20H05643, JP21K13957, JP21H04492, and JP24H00022, the ISEE director's leadership fund for FYs 2021 -- 2024, the Young Leader Cultivation (YLC) programme of Nagoya University, Tokai Pathways to Global Excellence (Nagoya University) of the Strategic Professional Development Program for

⁹ <https://www.aurorasaurus.org/>

¹⁰ <https://blog.aurorasaurus.org/?p=2030>

Young Researchers (MEXT), the young researcher units for the advancement of new and undeveloped fields in Nagoya University Program for Research Enhancement, and the NIHU Multidisciplinary Collaborative Research Projects NINJAL unit “Rediscovery of Citizen Science Culture in the Regions and Today”. This study was supported by the Research Council of Finland (projects 330063 QUASARE and 354280 GERACLIS). This work was partially funded by the Horizon Europe program projects ALBATROS and SPEARHEAD. We acknowledge the support of the International Space Science Institute (Bern, Switzerland) and International Team No. 585 (REASSESS). IPS observations were made under the solar wind program of the Institute for Space-Earth Environmental Research, Nagoya University.

We thank Yuichi Otsuka, Michi Nishioka, and Septi Perwitasari for developing and sharing the TEC codes. We thank Ilya Usoskin and Keith Ryden for their helpful discussions for the GLE #74. We thank Takuya Tsugawa, Mamoru Ishii, and Michi Nishioka for their valuable advice on the ionospheric disturbances at that time. We thank Elizabeth Macdonald and Vincent Ledvina for their helpful discussions on the citizen-science approach on the auroral records.

We thank Tony Philipps, Martin Snow, Cristina Mandrini, Andrew Lewis, Hong-Jin Yang, Jacques van Delft, Kazue Nakagawa, and Ichiro Ota for helping us distribute the said survey form for the local auroral visibility. We thank Frédéric Desmoulins, Carlos Matos, Angelica D. Vazquez Sepulveda, Rene Saade, Shiori Yamada, Ryu Tamura, Trent Davis, Joel Weatherly, Tina Booth, Laura-May Abron, Landon Oxford, Leyton Riley, David Batchelor, Víctor R. Ruiz, Yuto Hoshino, Kate Green, Karl Krammes, Huili Chai, Horace A Smith, Akihiro Tamura, Edwin Rivera, Alan Viles, Jeff Vollin, Stella Stritch, Sam Deutsch, Robert Stuart, John Bradshaw, Shigeki Tomita, M. L. Couprie, Ida Kraševc, Jesse Wall, Rosenberg Róbert, Tim Martin, Jimmie Strouhal, Tyler McLain, Greg Redfern, Michael Borman, Evan Saltman, Miriah Shadara, Helen Spillane, Jamie McBean, Graham Whittington, Clark Austin, Drew Medlin, Laura Lockhart, Larkyn Timmerman, Ricardo Muracciole, Laura Lockhart, Joël Van Quathem, Francisco Martinez Nieto, Gentrit Zenuni, Genna Chiaro, Joseph Giacinto, Vincent Ledvina, Paul D. Maley, Julia Sumerling, Denis Martínez, Brandon Flores, Yutaka Kagaya, Gerard Kelly Edgar Castro, Edy Yoc, Víctor M. S. Carrasco, Becky Gravelle, Miyuki Miyaji, Shunsuke Nozawa, Frank Garcia, Richard Payne, Ryosuke Takagi, Georg Woeber, and Mirko Piersanti for contributing their experience and photographs through the survey form.

References

- Akasofu, S. -I., Chao, J. K. 1980, Interplanetary shock waves and magnetospheric substorms, *Planetary and Space Science*, **28**, 381-385. DOI: 10.1016/0032-0633(80)90042-2
- Alken, P., Thébault, E., Beggan, C. D., *et al.* 2021, International Geomagnetic Reference Field: the thirteenth generation, *Earth, Planets and Space*, **73**, 49. DOI: 10.1186/s40623-020-01288-x
- Angelopoulos, V. 2008, The THEMIS mission. *Space Science Reviews*, **141**, 5–34. DOI: 10.1007/s11214-008-9336-1
- Araki, T. 1994, A Physical model of the geomagnetic sudden commencement, *Solar Wind Sources of Magnetospheric Ultra-Low-Frequency Waves*. Geophys. Monogr. Ser., vol. 81, edited by M. J. Engebreston, K. Takahashi, and M. Scholer, pp. 183-200, AGU, Washington, D. C. Pub Date: 1994 DOI: 10.1029/GM081p0183
- Araki, T., Keika, K., Kamei, T., Yang, H., Alex, S. 2006, Nighttime Enhancement of the Amplitude of Geomagnetic Sudden Commencements and its Dependence on IMF-Bz, *Earth, Planets and Space*, **58**, 45-50. DOI: 10.1186/BF03351912
- Araki, T. 2014, Historically Largest Geomagnetic Sudden Commencement (SC) since 1868, *Earth, Planets and Space*, **66**, 164. DOI: 10.1186/s40623-014-0164-0
- Auster, U., Glassmeier, K. H., Magnes, W., Aydogar, O., Baumjohann, W., Constaninescu, D., *et al.* 2008, The THEMIS fluxgate magnetometer, *Space Science Reviews*, **141**, 235–264. DOI: 10.1007/s11214-008-9365-9
- Baker, D. N., Balstad, R., Bodeau, M., *et al.* 2008, *Severe space weather events—understanding societal and economic impacts*, Washington DC, National Academies Press

- Baker, D. N., Erickson, P. J., Fennell, J. F., Foster, J. C., Jaynes, A. N., Verronen, P. T. 2017, Space Weather Effects in the Earth's Radiation Belts, *Space Science Reviews*, **24**, 1-60. DOI: 10.1007/s11214-017-0452-7
- Bechet, S., Clette, F. 2022, *uset_synoptic_images_L1centered*, <https://doi.org/10.24414/nc7j-b391>, Published by Royal Observatory of Belgium (ROB)
- Beggan, C. D., Beamish, D., Richards, A., Kelly, G. S., Thomson, A. W. P. 2013, Prediction of extreme geomagnetically induced currents in the UK high-voltage network, *Space Weather*, **11**, 407-419. DOI: 10.1002/swe.20065.
- Blake, S. P., Pulkkinen, A., Schuck, P. W., Glocer, A., Tóth, G. 2021, Estimating Maximum Extent of Auroral Equatorward Boundary Using Historical and Simulated Surface Magnetic Field Data, *Journal of Geophysical Research: Space Physics*, **126**, e28284. DOI: 10.1029/2020JA028284
- Bobra, M. G., Sun, X., Hoeksema, J. T., Turmon, M., Liu, Y., Hayashi, K., Barnes, G., Leka, K. D. 2014, The Helioseismic and Magnetic Imager (HMI) Vector Magnetic Field Pipeline: SHARPs - Space-Weather HMI Active Region Patches, *Solar Physics*, **289**, 3549-3578. DOI: 10.1007/s11207-014-0529-3
- Boteler, D. H. 2019, A 21st Century View of the March 1989 Magnetic Storm, *Space Weather*, **17**, 1427-1441. DOI: 10.1029/2019SW002278
- Brandt, P. C., Mitchell, D. G., Ebihara, Y., Sandel, B. R., Roelof, E. C., Burch, J. L., Demajistre, R. 2002, Global IMAGE/HENA observations of the ring current: Examples of rapid response to IMF and ring current-plasmasphere interaction, *Journal of Geophysical Research (Space Physics)*, **107**, 1359. DOI: 10.1029/2001JA000084
- Brueckner, G. E., Howard, R. A., Koomen, M. J., *et al.* 1995, The Large Angle Spectroscopic Coronagraph (LASCO), *Solar Physics*, **162**, 357-402. DOI: 10.1007/BF00733434
- Case, N. A., MacDonald, E. A., Viereck, R. 2016a, Using Citizen Science Reports to Define the Equatorial Extent of Auroral Visibility, *Space Weather*, **14**, 198-209. DOI: 10.1002/2015SW001320
- Case, N. A., Kingman, D., MacDonald, E. A. 2016, A real-time hybrid aurora alert system: Combining citizen science reports with an auroral oval model, *Earth and Space Science*, **3**, 257-265. DOI: 10.1002/2016EA000167
- Chamberlain, J. W. 1961, *Physics of the Aurora and Airglow*, New York, Academic Press
- Chapman, S. C., Dudok de Wit, T. 2024, A Solar Cycle Clock for Extreme Space Weather, *Scientific Reports*, **14**, 8249. DOI: 10.1038/s41598-024-58960-5
- Chapman, S. C., McIntosh, S. W., Leamon, R. J., Watkins, N. W. 2020, Quantifying the Solar Cycle Modulation of Extreme Space Weather, *Geophysical Research Letters*, **47**, e87795. DOI: 10.1029/2020GL087795
- Clette, F. 2011, Past and future sunspot indices: New goals for SoTerIA, *Journal of Atmospheric and Solar-Terrestrial Physics*, **73**, 182-186. DOI: 10.1016/j.jastp.2009.12.015
- Clette, F., Jain, S., Podladchikova, T. 2024, The McNish and Lincoln Solar-Activity Predictions: The Method and Its Performance, *Solar Physics*, **299**, 22. DOI: 10.1007/s11207-024-02266-2
- Clette, F., Lefèvre, L., Chatzistergos, T., *et al.* 2023, Recalibration of the Sunspot-Number: Status Report, *Solar Physics*, **298**, 44. DOI: 10.1007/s11207-023-02136-3
- Cliver, E. W., Schrijver, C. J., Shibata, K., Usoskin, I. G. 2022, Extreme Solar Events, *Living Reviews in Solar Physics*, **19**, 2. DOI: 10.1007/s41116-022-00033-8
- Cummings, W. D., Asymmetric ring currents and the low-latitude disturbance daily variation, *Journal of Geophysical Research*, **71**, 4495-4503. DOI: 10.1029/JZ071i019p04495.
- Daglis, I. A. 2001, *Space Storms and Space Weather Hazards*, Amsterdam, Kluwer
- David, M., Sojka, J. J., Schunk, R. W., Liemohn, M. W., Coster, A. J. 2011, Dayside midlatitude ionospheric response to storm time electric fields: A case study for 7 September 2002. *Journal of Geophysical Research*, **116**, A12302. DOI: 10.1029/2011JA016988
- Ebihara, Y., Ejiri, M., Nilsson, H., Sandahl, I., Milillo, A., Grande, M., Fennell, J., and Roeder, J. 2002, Statistical distribution of the storm-time proton ring current: POLAR measurements, *Geophysical Research Letters*, **29**, 1969, DOI: 10.1029/2002GL015430.
- Ebihara, Y., Fok, M. -C., Sazykin, S., Thomsen, M. F., Hairston, M. R., Evans, D. S., Rich, F. J.,

- Ejiri, M. 2005, Ring current and the magnetosphere-ionosphere coupling during the superstorm of 20 November 2003, *Journal of Geophysical Research: Space Physics*, **110**, A09S22. DOI: 10.1029/2004JA010924
- Ebihara, Y., Hayakawa, H., Iwahashi, K., Tamazawa, H., Kawamura, A.D., Isobe, H. 2017, Possible cause of extremely bright aurora witnessed in East Asia in September 1770, *Space Weather*, **15**, 1373-1382. DOI: 10.1002/2017SW001693
- Falchi, F., Cinzano, P., Duriscoe, D., Kyba, C. C. M., Elvidge, C. D., Baugh, K., Portnov, B. A., Rybnikova, N. A., Furgoni, R. 2016, The New World Atlas of Artificial Night Sky Brightness, *Science Advances*, **2**, e1600377-e1600377. DOI: 10.1126/sciadv.1600377
- Forbush, S. E. 1937, On the Effects in Cosmic-Ray Intensity Observed During the Recent Magnetic Storm, *Physical Review*, **51**, 1108–1109. DOI: 10.1103/PhysRev.51.1108.3
- Foster, J. C. 1989, Plasma transport through the dayside cleft: A source of ionization patches in the polar cap. In P. Sandholt & A. Egeland (Eds.), *Electromagnetic coupling in the polar clefts and caps* (pp. 343–354). Kluwer Academic.
- Foster, J. C. 1993, Storm-time plasma transport at middle and high latitudes. *Journal of Geophysical Research*, **98**, 1675–1689. DOI: 10.1029/92JA02032
- Ghosh, S. 2024, Sky Gazers Capture Rare Red Aurora from Himalayan Observatory, *Nature India*, DOI: 10.1038/d44151-024-00068-w
- Gopalswamy, N., Yashiro, S., Michalek, G., Stenborg, G., Vourlidas, A., Freeland, S., Howard, R. 2009, The SOHO/LASCO CME Catalog, *Earth, Moon, and Planets*, **104**, 295-313. DOI: 10.1007/s11038-008-9282-7
- Gopalswamy, N., Yashiro, S., Xie, H., Akiyama, S., Mäkelä, P. 2015, Properties and Geoeffectiveness of Magnetic Clouds during Solar Cycles 23 and 24, *Journal of Geophysical Research: Space Physics*, **120**, 9221-9245. DOI: 10.1002/2015JA021446
- Gopalswamy, N., Akiyama, S., Yashiro, S., Makela, P., Xie, H. 2024, Intense Geomagnetic Storms during Solar Cycles 23-25, in: Georgieva, K., Kirov, B., Asenovski, S. (eds.) *Proceedings of the Fifteenth Workshop Solar Influences on the Magnetosphere, Ionosphere and Atmosphere, June, 2023* (ISSN 2367-7570), Sofia, the Bulgarian Academy of Science; 47-55. Greshko, M. 2024, Extreme Solar Storm Generated Aurorae—and ‘Surprise’, *Science*, DOI: 10.1126/science.zoakd5z
- Hands, A. D. P., Ryden, K. A., Meredith, N. P., Glauert, S. A., & Horne, R. B. 2018, Radiation Effects on Satellites During Extreme Space Weather Events, *Space Weather*, **16**, 1216-1226. DOI: 10.1029/2018SW001913
- Hapgood, M., Angling, M. J., Attrill, G., *et al.* 2021, Development of Space Weather Reasonable Worst Case Scenarios for the UK National Risk Assessment, *Space Weather*, **19**, e02593. DOI: 10.1029/2020SW002593
- Hashimoto, K. K., Kikuchi, T., Ebihara, Y. 2002, Response of the magnetospheric convection to sudden interplanetary magnetic field changes as deduced from the evolution of partial ring currents, *Journal of Geophysical Research (Space Physics)*, **107**, 1337. DOI: 10.1029/2001JA009228
- Hayakawa, H., Bechet, S., Clette, F., Hudson, H., Maehara, H., Namekata, K., Notsu, Y. 2023c, Magnitude Estimates for the Carrington Flare in September 1859 as seen from the Original Records, *The Astrophysical Journal Letters*, **954**, L3. DOI: 10.3847/2041-8213/acd853
- Hayakawa, H., Cliver, E. W., Clette, F., Ebihara, Y., Toriumi, S., Ermolli, I., Chatzistergos, T., Hattori, K., Knipp, D. J., Blake, S. P., Cauzzi, G., Reardon, K., Bourdin, P.-A., Just, D., Vokhmyanin, M., Matsumoto, K., Miyoshi, Y., Ribeiro, J. R., Correia, A. P., Willis, D. M., Wild, M. N., Silverman, S. M. 2023b, The Extreme Space Weather Event of February 1872: Sunspots, Magnetic Disturbance, and Auroral Displays, *The Astrophysical Journal*, **959**, 23. DOI: 10.3847/1538-4357/acc6cc
- Hayakawa, H., Ebihara, Y., Hata, H. 2023a, A Review for Japanese auroral records on the three extreme space weather events around the International Geophysical Year (1957 – 1958), *Geoscience Data Journal*, **10**, 142-157. DOI: 10.1002/GDJ3.140
- Hayakawa, H., Ebihara, Y., Pevtsov, A. A. 2024, Analyses of Equatorward Auroral Extensions during the Extreme Geomagnetic Storm on 15 July 1959, *Monthly Notices of the Royal*

- Astronomical Society*, **527**, 7298-7305. DOI: 10.1093/mnras/stad3556
- Hayakawa, H., Oliveira, D. M., Shea, M. A., Smart, D. F., Blake, S. P., Hattori, K., Bhaskar, A. T., Curto, J. J., Franco, D. R., Ebihara, Y. 2022, The Extreme Solar and Geomagnetic Storms on 20-25 March 1940, *Monthly Notices of the Royal Astronomical Society*, **517**, 1709–1723. DOI: 10.1093/mnras/stab3615
- Hayakawa, H., Ribeiro, J. R., Ebihara, Y., Correira, A. P., Sôma, M. 2020, South American auroral reports during the Carrington storm, *Earth, Planets and Space*, **72**, 122. DOI: 10.1186/s40623-020-01249-4
- Hudson, H., Cliver, E., White, S., Machol, J., Peck, C., Tolbert, K., Viereck, R., Zarro, D. 2024, The Greatest GOES Soft X-ray Flares: Saturation and Recalibration over Two Hale Cycles, *Solar Physics*, **299**, 39. DOI: 10.1007/s11207-024-02287-x
- Inoue, S., Magara, T., Pandey, V. S., Shiota, D., Kusano, K., Choe, G. S., Kim, K. S. 2014, Nonlinear Force-free Extrapolation of the Coronal Magnetic Field Based on the Magnetohydrodynamic Relaxation Method, *The Astrophysical Journal*, **780**, 101. DOI: 10.1088/0004-637X/780/1/101
- INTERMAGNET *et al.*, 2021, Intermagnet Reference Data Set (IRDS) 2018 – Definitive Magnetic Observatory Data. GFZ Data Services. DOI: 10.5880/INTERMAGNET.1991.2018
- Iwai, K., Shiota, D., Tokumaru, M., Fujiki, K., Den, M., Kubo, Y. 2019, Development of a coronal mass ejection arrival time forecasting system using interplanetary scintillation observations, *Earth, Planets and Space*, **71**, 39. DOI: 10.1186/s40623-019-1019-5
- Iwai, K., Shiota, D., Tokumaru, M., Fujiki, K., Den, M., Kubo, Y. 2021, Validation of coronal mass ejection arrival-time forecasts by magnetohydrodynamic simulations based on interplanetary scintillation observations, *Earth, Planets and Space*, **73**, 9. DOI: 10.1186/s40623-020-01345-5
- Kakioka Magnetic Observatory 2013, Kakioka Geomagnetic Field 1-Minute Digital Data in IAGA-2002 Format, *Kakioka Magnetic Observatory Digital Data Service*, DOI: 10.48682/186bd.3f000
- Kakioka Magnetic Observatory, 2015, Kakioka Sudden Impulse and Storm Sudden Commencement Catalog [dataset], *Kakioka Magnetic Observatory Digital Data Service*, DOI: 10.48682/386bd.003d0
- Kamide, Y. The two-component auroral electrojet, *Geophysical Research Letters*, **9**, 1175-1178. DOI: 10.1029/GL009i010p01175
- Kamide, Y., Yokoyama, N., Gonzalez, W., Tsurutani, B. T., Daglis, I. A., Brekke, A., Masuda, S. 1998, Two-step development of geomagnetic storms, *Journal of Geophysical Research*, **103**, 6917-6922. DOI: 10.1029/97JA03337
- Karimov, K., Lee, H., Jeong, H.-J., Moon, Y.-J., Kang, J., Son, J., Jeon, M., Kusano, K. 2024, 3D Magnetic Free Energy and Flaring Activity Using 83 Major Solar Flares, *The Astrophysical Journal Letters*, **965**, L5. DOI: 10.3847/2041-8213/ad3548 ApJ 965:L5 (2024)
- Kilpua, E. K. J., Olsper, N., Grigorievskiy, A., K pyl , M. J., Tanskanen, E. I., Miyahara, H., Kataoka, R., Pelt, J., Liu, Y. D. 2015, Statistical Study of Strong and Extreme Geomagnetic Disturbances and Solar Cycle Characteristics, *The Astrophysical Journal*, **806**, 272. DOI: 10.1088/0004-637X/806/2/272
- Klein, K.-L., Dalla, S. 2017, Acceleration and Propagation of Solar Energetic Particles, *Space Science Reviews*, **212**, 1107-1136. DOI: 10.1007/s11214-017-0382-4
- Klein, K.-L., Musset, S., Vilmer, N., Briand, C., Krucker, S., Francesco B. A., Dresing, N., Palmroos, C., Gary, D. E. 2022, The Relativistic Solar Particle Event on 28 October 2021: Evidence of Particle Acceleration within and Escape from the Solar Corona, *Astronomy & Astrophysics*, **663**, A173. DOI: 10.1051/0004-6361/202243903
- Knipp, D. J., Bernstein, V., Wahl, K., Hayakawa, H. 2021, Timelines as a tool for learning about space weather storms, *Journal of Space Weather and Space Climate*, **11**, 29. DOI: 10.1051/swsc/2021011
- Koons, H. C., & Fennell, J. F. (2006). Space weather effects on communications satellites. *The Radio Science Bulletin*, 2006(316), 27-41. DOI: 10.23919/URSIRSB.2006.790935
- Kosar, B. C., MacDonald, E. A., Case, N. A., Heavner, M. 2018a, Aurorasaurus Database of Real-

- Time, Crowd-Sourced Aurora Data for Space Weather Research, *Earth and Space Science*, **5**, 970-980. DOI: 10.1029/2018EA000454
- Kosar, B. C., MacDonald, E. A., Case, N. A., Zhang, Y., Mitchell, E. J., Viereck, R. 2018b, A case study comparing citizen science aurora data with global auroral boundaries derived from satellite imagery and empirical models, *Journal of Atmospheric and Solar-Terrestrial Physics*, **177**, 274-282. DOI: 10.1016/j.jastp.2018.05.006
- Kozyra, J. U., Nagy, A. F., Slater, D. W. 1997, High-Altitude Energy Source(s) for Stable Auroral Red Arcs, *Reviews of Geophysics*, **35**, 155-190. DOI: 10.1029/96RG03194
- Kress, B. T., et al., 2021, Observations From NOAA's Newest Solar Proton Sensor, *Space Weather*, **19**, e2021SW002750. DOI: 10.1029/2021SW002750
- Kudela, K., Bučík, R., Bobík, P. 2008, On Transmissivity of Low Energy Cosmic Rays in Disturbed Magnetosphere, *Advances in Space Research*, **42**, 1300-1306. DOI: 10.1016/j.asr.2007.09.033
- Kusano, K., Iju, T., Bamba, Y., Inoue, S. 2020, A physics-based method that can predict imminent large solar flares, *Science*, **369**, 587-591. DOI: 10.1126/science.aaz2511
- Kusano, K. 2023, *Solar-Terrestrial Environmental Prediction*, Singapore: Springer Nature Singapore
- Laundal, K. M., Richmond, A. D. 2017, Magnetic Coordinate System, *Space Science Review*, **206**, 27-59. DOI: 10.1007/s11214-016-0275-y
- Le, G., Russell, C. T., and Takahashi, K. 2004, Morphology of the ring current derived from magnetic field observations, *Annales Geophysicae*, **22**, 1267-1295, DOI: 10.5194/angeo-22-1267-2004.
- Lefèvre, L., Vennerstrøm, S., Dumbović, M., Vršnak, B., Sudar, D., Arlt, R., Clette, F., Crosby, N. 2016, Detailed Analysis of Solar Data Related to Historical Extreme Geomagnetic Storms: 1868 - 2010, *Solar Physics*, **291**, 1483-1531. DOI: 10.1007/s11207-016-0892-3
- Lemen, J. R., Title, A. M., Akin, D. J., et al. 2012, The Atmospheric Imaging Assembly (AIA) on the Solar Dynamics Observatory (SDO), *Solar Physics*, **275**, 17-40. DOI: 10.1007/s11207-011-9776-8
- Li, L., Jin, S. 2024, Ionospheric behaviors and characteristics in Asian sector during the April 2023 geomagnetic storm with multi-instruments observations, *Journal of Atmospheric and Solar-Terrestrial Physics*, **259**, 106238. DOI: 10.1016/j.jastp.2024.106238
- Liu, Y. D., Hu, H., Wang, R., et al. 2015, Plasma and Magnetic Field Characteristics of Solar Coronal Mass Ejections in Relation to Geomagnetic Storm Intensity and Variability, *The Astrophysical Journal Letters*, **809**, L34. DOI: 10.1088/2041-8205/809/2/L34
- Lummerzheim, D., Galand, M., Semeter, J., Mendillo, M. J., Rees, M. H., Rich, F. J. 2001, Emission of O I(630 nm) in Proton Aurora, *Journal of Geophysical Research*, **106**, 141-148 DOI: 10.1029/2000JA002005
- MacDonald, E. A., Case, N. A., Clayton, J. H., Hall, M. K., Heavner, M., Lalone, N., Patel, K. G., Tapia, A. 2015, Aurorasaurus: A citizen science platform for viewing and reporting the aurora, *Space Weather*, **13**, 548-559. DOI: 10.1002/2015SW001214
- Manu, V., Balan, N., Zhang, Q. -H., Xing, Z. -Y. 2022, Association of the Main Phase of the Geomagnetic Storms in Solar Cycles 23 and 24 With Corresponding Solar Wind-IMF Parameters, *Journal of Geophysical Research: Space Physics*, **127**, e2022JA030747. DOI: 10.1029/2022JA030747
- Matzka, J., Stolle, C., Yamazaki, Y., Bronkalla, O., Morschhauser, A. 2021, The Geomagnetic Kp Index and Derived Indices of Geomagnetic Activity, *Space Weather*, **19**, e2020SW002641. DOI: 10.1029/2020SW002641
- Mavromichalaki, H., Papaioannou, A., Plainaki, C., et al. 2011, Applications and Usage of the Real-Time Neutron Monitor Database, *Advances in Space Research*, **47**, 2210-2222. DOI: 10.1016/j.asr.2010.02.019
- McFadden, J. P., Carlson, C. W., Larson, D., Ludlam, M., Abiad, R., Elliott, B., et al. 2008, The THEMIS ESA plasma instrument and in-flight calibration, *Space Science Reviews*, **141**, 277-302. DOI: 10.1007/s11214-008-9440-2
- McIlwain, C. E. 1961, Coordinates for Mapping the Distribution of Magnetically Trapped Particles,

- Journal of Geophysical Research*, **66**, 3681-3691. DOI: 10.1029/JZ066i011p03681
- McIntosh, S. W., Chapman, S., Leamon, R. J., Egeland, R., Watkins, N. W. 2020, Overlapping Magnetic Activity Cycles and the Sunspot Number: Forecasting Sunspot Cycle 25 Amplitude, *Solar Physics*, **295**, 163. DOI: 10.1007/s11207-020-01723-y
- Meel, P., Vishwakarma, D. K. 2020, Fake news, rumor, information pollution in social media and web: A contemporary survey of state-of-the-arts, challenges and opportunities, *Expert Systems with Applications*, **153**, 112986. DOI: 10.1016/j.eswa.2019.112986
- Mendillo, M., Finan, R., Baumgardner, J., Wroten, J., Martinis, C., and Casillas, M. 2016, A stable auroral red (SAR) arc with multiple emission features, *Journal of Geophysical Research: Space Physics*, **121**, 10,564–10,577, DOI: 10.1002/2016JA023258.
- Mishev, A. L., Kocharov, L. G., Usoskin, I. G. 2014, Analysis of the Ground Level Enhancement on 17 May 2012 Using Data from the Global Neutron Monitor Network, *Journal of Geophysical Research: Space Physics*, **119**, 670-679. DOI: 10.1002/2013JA019253
- Mishev, A. L., Kocharov, L. G., Koldobskiy, S. A., Larsen, N., Riihonen, E., Vainio, R., Usoskin, I. G. 2021, High-Resolution Spectral and Anisotropy Characteristics of Solar Protons During the GLE N°73 on 28 October 2021 Derived with Neutron-Monitor Data Analysis, *Solar Physics*, **297**, 88. DOI: 10.1007/s11207-022-02026-0
- Mishev, A., Usoskin, I., Raukunen, O., Paassilta, M., Valtonen, E., Kocharov, L., Vainio, R. 2018, First Analysis of Ground-Level Enhancement (GLE) 72 on 10 September 2017: Spectral and Anisotropy Characteristics, *Solar Physics*, **293**, 136. DOI: 10.1007/s11207-018-1354-x
- Miyake, F., Usoskin, I. G., Poluianov, S. 2019, *Extreme Solar Particle Storms; The Hostile Sun*, Bristol, IOP.
- Miyaoka, H., Hirasawa, T., Yumoto, K., Tanaka, Y. 1990, Low Latitude Aurorae on October 21, 1989. I, *Proceedings of the Japan Academy, Series B*, **66**, 47-51. DOI: 10.2183/pjab.66.47
- Nakamura, M., Yoneda, A., Oda, M., Tsubouchi, K. 2015, Statistical analysis of extreme auroral electrojet indices, *Earth, Planets and Space*, **67**, 153. DOI: 10.1186/s40623-015-0321-0
- Newell, P. T., Feldstein, Y. I., Galperin, Y. I., Meng, C.-I. 1996, Morphology of Nightside Precipitation, *Journal of Geophysical Research*, **101**, 10737-10748. DOI: 10.1029/95JA03516
- Newell, P. T., Gjerloev, J. W. 2011, Evaluation of SuperMAG auroral electrojet indices as indicators of substorms and auroral power, *Journal of Geophysical Research*, **116**, A12211, doi:10.1029/2011JA016779.
- Nishida, A. 1968, Coherence of geomagnetic DP 2 fluctuations with interplanetary magnetic variations. *Journal of Geophysical Research*, **73**, 5549–5559. DOI: 10.1029/JA073i017p05549
- Ohtani, S., Wing, S., Newell, P. T., Higuchi, T. 2010, Locations of night-side precipitation boundaries relative to R2 and R1 currents, *Journal of Geophysical Research*, **115**, A10233. DOI: 10.1029/2010JA015444
- Oliveira, D. M., Weygand, J. M., Zesta, E., Ngwira, C. M., Hartinger, M. D., Xu, Z., Giles, B. L., Gershman, D. J., Silveira, M. V. D., & Souza, V. M. (2021). Impact angle control of local intense dB/dt variations during shock-induced substorms. *Space Weather*, **19**, e2021SW002933. DOI: 10.1029/2021SW002933
- Owens, M. J., Lockwood, M., Barnard, L. A., Scott, C. J., Haines, C., Macneil, A. 2022, Extreme Space-Weather Events and the Solar Cycle, *Solar Physics*, **296**, 82. DOI: 10.1007/s11207-021-01831-3
- Papaoannou, A., Kouloumvakos, A., Mishev, A., Vainio, R., Usoskin, I., Herbst, K., Rouillard, A. P., Anastasiadis, A., Gieseler, J., Wimmer-Schweingruber, R., Kühl, P. 2022, The First Ground-Level Enhancement of Solar Cycle 25 on 28 October 2021, *Astronomy & Astrophysics*, **660**, L5. DOI: 10.1051/0004-6361/202142855
- Papitashvili, N. E., King, J. H. 2020, OMNI 5-min Data [Data set], NASA Space Physics Data Facility, DOI: 10.48322/gbpg-5r77, Accessed on 2024-07-02.
- Pesnell, W. D. 2016, Predictions of Solar Cycle 24: How are we doing? *Space Weather*, **14**, 10-21. DOI: 10.1002/2015SW001304
- Pesnell, W. D. 2020, Lessons learned from predictions of Solar Cycle 24, *Journal of Space Weather*

- and Space Climate*, **10**, 60. DOI: 10.1051/swsc/2020060
- Pesnell, W. D., Schatten, K. H. 2018, An Early Prediction of the Amplitude of Solar Cycle 25, *Solar Physics*, **293**, 112. DOI: 10.1007/s11207-018-1330-5
- Piersanti, M., Cesaroni, C., Spogli, L., Alberti, T. 2017, Does TEC React to a Sudden Impulse as a Whole? The 2015 Saint Patrick's Day Storm Event, *Advances in Space Research*, **60**, 1807-1816. DOI: 10.1016/j.asr.2017.01.021
- Poluianov, S. V., Usoskin, I. G., Mishev, A. L., Shea, M. A., Smart, D. F. 2017, GLE and Sub-GLE Redefinition in the Light of High-Altitude Polar Neutron Monitors, *Solar Physics*, **292**, 176. DOI: 10.1007/s11207-017-1202-4
- Pulkkinen, T. 2007, Space Weather: Terrestrial Perspective, *Living Reviews in Solar Physics*, **4**, 1. DOI: 10.12942/lrsp-2007-1
- Rees, M. H. 1961, Excitation of High Altitude Red Auroral Arcs, *Planetary and Space Science*, **8**, 59-67. DOI: 10.1016/0032-0633(61)90156-8
- Rees, M. H., Deehr, C. S., 1961, The aurora of 27 November 1959 at College, Alaska, including observations of a high altitude red arc, *Planetary Space Science*, **8**, 49-58, DOI: 10.1016/0032-0633(61)90155-6
- Riley, P., Baker, D., Liu, Y. D., Verronen, P., Singer, H., Güdel, M. 2018, Extreme Space Weather Events: From Cradle to Grave, *Space Science Reviews*, **214**, 21. DOI: 10.1007/s11214-017-0456-3
- Roach, F. E., Moore, J. G., Bruner, E. C., Jr., Cronin, H., Silverman, S. M. 1960, The Height of Maximum Luminosity in an Auroral Arc, *Journal of Geophysical Research*, **65**, 3575-3580. DOI: 10.1029/JZ065i011p03575
- Scolini, C., Chané, E., Temmer, M., Kilpua, E. K. J., Dissauer, K., Veronig, A. M., Palmerio, E., Pomoell, J., Dumbović, M., Guo, J., Rodriguez, L., Poedts, S. 2020, CME-CME Interactions as Sources of CME Geoeffectiveness: The Formation of the Complex Ejecta and Intense Geomagnetic Storm in 2017 Early September, *The Astrophysical Journal Supplement Series*, **247**, 21. DOI: 10.3847/1538-4365/ab6216
- Shinbori, A., Otsuka, Y., Tsugawa, T., et al. 2019, Temporal and Spatial Variations of Storm Time Midlatitude Ionospheric Trough Based on Global GNSS-TEC and Arase Satellite Observations, *Geophysical Research Letters*, **45**, 7362-7370. DOI: 10.1029/2018GL078723
- Shinbori, A., Otsuka, Y., Sori, T., Tsugawa, T., Nishioka, M. 2020, Temporal and spatial variations of total electron content enhancements during a geomagnetic storm on 27 and 28 September 2017. *Journal of Geophysical Research*, **125**, e2019JA026873. DOI: 10.1029/2019JA026873
- Shinbori, A., Otsuka, Y., Sori, T., Tsugawa, T., Nishioka, M. 2022, Statistical Behavior of Large-Scale Ionospheric Disturbances From High Latitudes to Mid-Latitudes During Geomagnetic Storms Using 20-yr GNSS-TEC Data: Dependence on Season and Storm Intensity, *Journal of Geophysical Research: Space Physics*, **127**, e29687. DOI: 10.1029/2021JA029687
- Shinbori, A., Tsuji, Y., Kikuchi, T., Araki, T., Ikeda, A., Uozumi, T., Baishev, D., Shevtsov, B. M., Nagatsuma, T., Yumoto, K. 2012, Magnetic Local Time and Latitude Dependence of Amplitude of the Main Impulse (MI) of Geomagnetic Sudden Commencements and its Seasonal Variation, *Journal of Geophysical Research: Space Physics*, **117**, A08322. DOI: 10.1029/2012JA018006
- Shinbori, A., Tsuji, Y., Kikuchi, T., Araki, T., Watari, S. 2009, Magnetic Latitude and Local Time Dependence of the Amplitude of Geomagnetic Sudden Commencements, *Journal of Geophysical Research*, **114**, A04217. DOI: 10.1029/2008JA013871
- Shiokawa, K., Meng, C. -I., Reeves, G. D., Rich, F. J., Yumoto, K. 1997, A Multievent Study of Broadband Electrons Observed by the DMSP Satellites and their Relation to Red Aurora Observed at Midlatitude Stations, *Journal of Geophysical Research*, **102**, 14237-14254. DOI: 10.1029/97JA00741
- Shiokawa, K., Ogawa, T., Kamide, Y. 2005, Low-Latitude Auroras Observed in Japan: 1999-2004, *Journal of Geophysical Research: Space Physics*, **110**, A05202. DOI: 10.1029/2004JA010706
- Shiota, D., Kataoka, R. 2016, Magnetohydrodynamic simulation of interplanetary propagation of multiple coronal mass ejections with internal magnetic flux rope (SUSANOO-CME), *Space*

- Weather*, **14**, 56-75. DOI: 10.1002/2015SW001308
- Smith, M. 2009, Time to Turn off the Lights, *Nature*, **457**, 27. DOI: 10.1038/457027a
- Solomon, S. C., Hays, P. B., Abreu, V. J. 1988, The auroral 6300 Å emission: Observations and modeling, *Journal of Geophysical Research*, **93**, 9867–9882. DOI: 10.1029/JA093iA09p09867
- Temmer, M. 2022, Space Weather: the Solar Perspective, *Living Reviews in Solar Physics*, **18**, 4. DOI: 10.1007/s41116-021-00030-3
- Terada, N., Iyemori, T., Nosé, M., Nagai, T., Matsumoto, H., Goka, T. 1998, Storm-time magnetic field variations observed by the ETS-VI satellite, *Earth Planets Space*, **50**, 853–864, DOI: 10.1186/bf03352179.
- Tokumar, M., Kojima, M., Fujiki, K., Maruyama, K., Maruyama, Y., Ito, H., Iju, T. 2011, A newly developed UHF radiotelescope for interplanetary scintillation observations: Solar Wind Imaging Facility, *Radio Science*, **46**, RS0F02. DOI: 10.1029/2011RS004694
- Tsubouchi, K., Omura, Y. 2007, Long-Term Occurrence Probabilities of Intense Geomagnetic Storm Events, *Space Weather*, **5**, S12003. DOI: 10.1029/2007SW000329
- Tsurutani, B. T., Zhou, X.-Y. 2003, Interplanetary shock triggering of substorms: Wind and Polar. *Advances in Space Research*, **31**, 1063–1067. DOI: 10.1016/S0273-1177(02)00796-2
- Turner, D. L., Shprits, Y., Hartinger, M., Angelopoulos, V. 2012, Explaining sudden losses of outer radiation belt electrons during geomagnetic storms. *Nature Physics*, **8**, 208-212. DOI: 10.1038/nphys2185
- Usoskin, I. G. 2023, A History of Solar Activity over Millennia, *Living Reviews in Solar Physics*, **20**, 2. DOI: 10.1007/s41116-023-00036-z
- Usoskin, I., Koldobskiy, S., Kovaltsov, G. A., Gil, A., Usoskina, I., Willamo, T., Ibragimov, A. 2020, Revised GLE database: Fluences of solar energetic particles as measured by the neutron-monitor network since 1956, *Astronomy & Astrophysics*, **640**, A17. DOI: 10.1051/0004-6361/202038272
- Usoskin, I., Miyake, F., Baroni, M., et al. 2023, Extreme Solar Events: Setting up a Paradigm, *Space Science Reviews*, **219**, 73. DOI: 10.1007/s11214-023-01018-1
- Watari, S. 2017, Geomagnetic Storms of Cycle 24 and their Solar Sources, *Earth, Planets and Space*, **69**, 70. DOI: 10.1186/s40623-017-0653-z
- WDC for Geomagnetism at Kyoto 2020, *Data Catalogue No. 32*, Kyoto, WDC for Geomagnetism at Kyoto
- WDC for Geomagnetism at Kyoto, Nose, M., Iyemori, T., Sugiura, M., Kamei, T. 2015a, *Geomagnetic Dst Index*, DOI: 10.17593/14515-74000.
- WDC for Geomagnetism at Kyoto, Nose, M., Iyemori, T., Sugiura, M., Kamei, T. 2015b, *Geomagnetic AE Index*, DOI: 10.17593/15031-54800.
- Webb, D., Nitta, N. 2017, Understanding Problem Forecasts of ISEST Campaign Flare-CME Events, *Solar Physics*, **292**, 142. DOI: 10.1007/s11207-017-1166-4
- Yamazaki, Y., Matzka, J., Siqueira da Silva, M. V., Kervalishvili, G. N., Korte, M., Rauberg, J. 2024, Assessment of Geomagnetic Activity for the Kp=9 “Gannon Storm” in May 2024 Based on Version 3.0 Hpo Indices, *ESS Open Archive*, DOI: 10.22541/essoar.171838396.68563140/v1
- Yokoyama, N., Kamide, Y., Miyaoka, H. 1998, The size of the auroral belt during magnetic storms, *Annales Geophysicae*, **16**, 566-573. DOI: 10.1007/s00585-998-0566-z
- Young, A. T. 1971, Interpretation of interplanetary scintillations, *The Astrophysical Journal*, **168**, 543-562. DOI: 10.1086/151108
- Yashiro, S., Gopalswamy, N., Michalek, G., St. Cyr, O. C., Plunkett, S. P., Rich, N. B., Howard, R. A. 2004, A Catalog of White Light Coronal Mass Ejections Observed by the SOHO Spacecraft, *Journal of Geophysical Research: Space Physics*, **109**, A07105. DOI: 10.1029/2003JA010282
- Zhang, T., Ebihara, Y., Tanaka, T. 2023, Nighttime Geomagnetic Response to Jumps of Solar Wind Dynamic Pressure: A Possible Cause of Québec Blackout in March 1989, *Space Weather*, **21**, e2023SW003493. DOI: 10.1029/2023SW003493